Modelling firn density at Dye-2 and KAN_U, two sites in the percolation zone of the Greenland ice sheet

Xueyu Zhang[1, 2], Lin Liu[1, 2*], Brice Noël[3], and Zhicai Luo[1, 2]

[1]MOE Key Laboratory of Fundamental Physical Quantities Measurement and Hubei Key Laboratory of Gravitation and Quantum Physics, PGMF and School of Physics, Huazhong University of Science and Technology, Wuhan 430074, P. R. China

[2]Institute of Geophysics and PGMF, Huazhong University of Science and Technology, Wuhan 430074, P. R. China

[3]Laboratoire de Climatologie et Topoclimatologie, University of Liège, Liège, Belgium

Correspondence to: Lin Liu (liulin616@hust.edu.cn)

Abstract. Modelling firn density is crucial for understanding the current mass balance of the Greenland ice sheet (GrIS) and predicting its future. As snowmelt increases in a warming climate on the GrIS, accurate information about firn density and its variability over time and space becomes increasingly important in the percolation zone. Previous research indicates that none of the existing models accurately simulate firn properties at sites with varying snowmelt rates due to the limited knowledge of liquid water percolation and the complexity of firn densification. Here, we enhance the representation of the firn densification model based on the Community Firn Model (CFM) by (i) using the stressed-based dry-firn densification scheme and recently published parametrizations for firn characteristics, (ii) modifying the expression of irreducible water in the Darcy-flow scheme, and (iii) allowing the time step to be adaptive. The improved model is employed at two climatologically distinct sites, Dye-2 and KAN_U, two sites in the southwest percolation zone of the GrIS, to evaluate its performance. The modelled firn depth-density profiles at the two study sites generally agree well with the in situ measurements obtained from 16 firn cores drilled between 2012 and 2019. At Dye-2, with comparatively high accumulation and low snowmelt rates, the model simulates thin ice lenses and/or ice layers in the top 10 m of the firn column. The modelled firn density aligns with the average level of observations, with the relative bias in density ranging from 0.36% to 6%. At the KAN_U site, characterized by relatively low accumulation and high snowmelt rates, the model captures high-density layers (~917 $kg \cdot m^{-3}$) caused by the refreezing of liquid water. The observed ice slabs are partly reproduced, and the relative bias in density between simulations and observations at all 8 cores is within ±5%.

1 Introduction

Accurate information about firn density and its variability over time and space is necessary both to understand the current mass balance of the Greenland ice sheet (GrIS) and to predict its future for multiple reasons. Firstly, firn depth and density are required to convert elevation (volume) changes measured from satellite altimetry to mass changes, which remains a

primary source of uncertainty in mass balance assessments (Shepherd et al., 2012, 2020; Huss et al., 2013; Thompson et al., 2023). Secondly, firn depth and density are required to convert firn column thickness to ice thickness to calculate solid-ice discharge over the grounding line (Rignot et al., 2019; Veldhuijsen et al., 2023). Thirdly, firn density and spatial distribution are required to calculate the amount of air-filled pore space within the firn column (firn air content; FAC), which implies the

35   meltwater retention potential and the capacity of firn to buffer surface meltwater into the ocean (Enderlin et al., 2014; Machguth et al., 2016; van den Broeke et al., 2016; Mottram et al., 2019). Moreover, the FAC of the total firn column is also valuable for remotely sensed surface height change correction, enabling the conversion of height changes into mass changes (Sørensen et al., 2011; Simonsen et al., 2013; Kuipers Munneke et al., 2015). Given the absence of suitable methodologies or techniques for directly measuring firn depth and density throughout the GrIS, firn densification models are typically used to

40   obtain vertical variations in density at a particular time and space (Ligtenberg et al., 2011; Morris and Wingham, 2015; Smith et al., 2020).

The surface of the GrIS can be divided into the accumulation zone and the ablation zone based on the equilibrium line altitude (ELA), with the accumulation zone further divided into the dry snow zone and the percolation zone depending on the

45   presence of liquid water (Steger et al., 2017). The dry snow zone is not affected by snowmelt and/or rainfall, and firn densification in this zone is forced by overburden stress, i.e. the weight of overlying snow/firn (Herron and Langway, 1980). In the GrIS, this zone is decreasing because areas experiencing snowmelt and/or rainfall have become more widespread and denser in response to the warming climate over the past decades. For example, an unprecedented melt event occurred in July 2012, with surface melt encompassing nearly the entire GrIS (Nghiem et al., 2012). As a result, the percolation zone of the

50   GrIS is expanding. Most liquid water (from snowmelt and rainfall) tends to infiltrate into the subsurface firn column in this zone. Afterwards, it may either be stored in the firn's pore space (Pfeffer et al., 1991; Harper et al., 2012), or refreeze within the firn layer (van den Broeke et al., 2016), or remain unfrozen in firn aquifers (Forster et al., 2014), or depart from the firn column via runoff when encountering an impermeable layer (Machguth et al., 2016). Researchers found sharply increased firn density and significant density variability within the upper firn column of the percolation zone (Machguth et al., 2016;

55   MacFerrin et al., 2019; Rennermalm et al., 2021), which are likely attributed to the refreezing of liquid water. This refreezing process produces ice lenses (thinner than 0.1 m) or ice layers (between 0.1 and 1 m thick), both of which can accumulate into ice slabs (thicker than 1 m) (MacFerrin et al., 2022), primarily influencing firn properties in two ways. Firstly, the release of latent heat during refreezing has the potential to induce a notable increase in firn temperature, further accelerating the rate of firn densification. Secondly, stress exerted by ice lenses or ice layers further compresses and densifies firn, thus leading to a

60   higher density within the firn layer. Furthermore, refreezing potentially acts as a buffer against meltwater entering the ocean,

delaying mass loss through runoff (Harper et al., 2012). Understanding refreezing processes is therefore critical for simulating firn density in the percolation zone, estimating the GrIS's mass loss and its influence on global sea-level rise.

Numerous semi-empirical and physics-based firn models have been developed to simulate firn properties and compared well
65   with observations on both Greenland and Antarctica (e.g. Arthern et al., 2010; Ligtenberg et al., 2011; Kuipers Munneke et al., 2015; van Kampenhout et al., 2017). However, the agreement between observed and simulated firn densities decreases with the increasing snowmelt rates (Kuipers Munneke et al., 2015; Ligtenberg et al., 2018), indicating that firn density modelling in the percolation zone remains a challenge. Many observational studies have demonstrated that meltwater infiltrates into the firn through two pathways, namely by homogeneous wetting front, also known as matrix flow, and by
70   heterogeneous infiltration in the form of discrete vertical channels, also called preferential flow (Pfeffer et al., 1996; Humphrey et al., 2012). Verjans et al. (2019) indicated that substantial knowledge gaps and poor representation of firn percolation processes are significant limiting factors in firn model performance in the percolation zone. Vandecrux et al. (2020c) found that none of the nine firn densification models accurately simulated meltwater infiltration at sites with varying snowmelt rates. Thompson et al. (2023) used two firn models (the SNOWPACK model and the CFM-GSFC model) to
75   quantify firn properties across the GrIS and found that the model bias is highest where liquid water is abundant.

In this study, we use the Community Firn Model (CFM; Stevens et al., 2020) as the modelling framework to simulate the firn depth-density profile in two climatologically distinct sites in the percolation zone of the GrIS: one characterized by relatively low accumulation and high snowmelt rates (KAN_U) and the other by comparatively high accumulation and low snowmelt
80   rates (Dye-2). The representation of firn densification is improved by (i) using the stressed-based dry-firn densification scheme and recently published parametrizations for surface density and thermal conductivity, (ii) modifying the expression of the irreducible water in the Darcy-flow scheme to assess the capillary retention, refreezing, and runoff of liquid water within the firn layer, and (iii) allowing the time step to be adaptive. The upper boundary of the model is driven by the polar version of the Regional Atmospheric Climate Model (RACMO2.3p2; Noël et al., 2019). In Sect. 4, We assess the overall
85   capability of the model to reproduce density profiles by comparing the modelled firn density with observations obtained from the nearest core with a length exceeding 10 m. In addition, we compare the simulation results with previous firn density modelling studies at Dye-2 and KAN_U by qualitatively and/or quantitatively comparing them with firn density observations, respectively. Finally, the sensitivity of the firn densification model to the choice of dry-firn compaction schemes, water flow schemes, and time step sizes are analyzed and discussed.

2 Data

2.1 Climatic forcing

The climatic forcing data of the model used in this study are snow mass accumulation (snowfall minus sublimation), liquid water flux (snowmelt plus rainfall), skin temperature, and 2 m air temperature. Rainfall is the difference between total precipitation and snowfall. Restricted by the availability of observational data in terms of time and space, these climatic data are typically collected from regional climate models (RCMs). The RCMs commonly employed for the investigation of meteorological and climatic characteristics of the GrIS involve RACMO2.3p2 (the Regional Atmospheric Climate Model version 2.3p2), MAR (the Modèle Atmosphérique Régional), PROMICE (Programme for Monitoring of the Greenland Ice Sheet), and HIRHAM (the High-Resolution Limited-Area Model). By comparing these RCMs to in situ meteorological data and point SEB/SMB measurements, the accuracy of RACMO2.3p2 is higher than the other models over the GrIS (Noël et al., 2018; Fettweis et al., 2020; Van Dalum et al., 2021). The forcing from RACMO2.3p2 has been demonstrated to yield significant improvements in modelled firn densification (Ligtenberg et al., 2018). Therefore, in order to precisely simulate the firn depth-density profiles, the atmospheric forcing of the model is collected from RACMO2.3p2 in this study.

RACMO2.3p2 is forced at the lateral boundaries by a combination of European Centre for Medium-Range Weather Forecasts (ECMWF) reanalysis datasets from ERA-40 over 1958-1978, ERA-Interim over 1979-1989, and ERA5 over 1990-2020 (Noël et al., 2019). The data of snowfall, snowmelt, total precipitation, sublimation, and 2 m air temperature are statistically downscaled on a daily basis from RACMO2.3p2 at 5.5 km resolution onto a 1 km grid for the period 1958-2020. In addition, skin temperature is available on a daily basis for the same time period but on the native RACMO2.3p2 grid at 5.5 km.

2.2 Study sites

In this study, case studies are conducted at Dye-2 (66.48° N, 46.28° W) and KAN_U (67.00° N, 47.02° W), two typical study sites in the percolation zone of the southwest GrIS (Fig. 1). Table 1 summarizes the geographical and climatological information of the two study sites. Situated in the southwest and at a lower elevation, KAN_U experiences a slightly higher annual mean surface temperature (-16.79℃) than Dye-2 (-18.34℃) between 1958 and 2020, resulting in higher snowmelt rates. Specifically, KAN_U exhibits an annual mean snowmelt of 282.83 mm w.e. (water equivalent) during this period, and meanwhile, Dye-2 display corresponding values of 145.97 mm w.e. With the increase in surface temperature of the GrIS over the past two decades, both snowfall and snowmelt have changed. A slight reduction in accumulation and an increase in snowmelt have been observed in KAN_U since 2008 (Fig. 2). In particular, the annual snowmelt exceeded the annual

accumulation in the warm years of 2010, 2012, 2016, and 2019. As a slightly warm site, the annual snowmelt at Dye-2

120   typically fluctuates between 32.42 and 310.56 mm w.e., except for the exceptionally high melt year of 2012, during which

the annual snowmelt exceeded the annual mass accumulation.
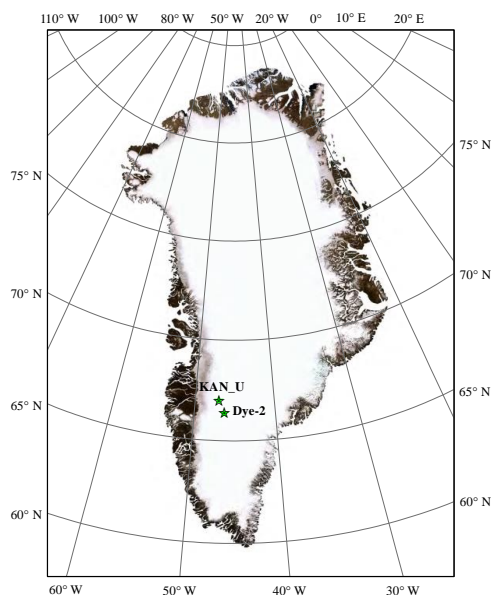
Figure 1. The geographical information of Dye-2 and KAN_U on the Greenland Ice Sheet.

125

Table 1. The climatological information about the two study sites. The annual mean surface temperature, accumulation and snowmelt are calculated on the basis of the RACMO2.3p2 model for the period from 1958 to 2020.

Site	Latitude (°)	Longitude (°)	Elevation (m)	Annual mean surface temperature (℃)	Annual mean accumulation (mm w.e.)	Annual mean snowmelt (mm w.e.)
Dye-2	66.48	-46.28	2119	-18.34	426.32	145.79
KAN_U	67.00	-47.02	1840	-16.79	463.38	282.83

130   Characterized by distinct climatic conditions, the control mechanism of firn densification differs in these two sites. High

accumulation and moderate snowmelt at Dye-2 make it a representative percolation zone. The firn densification at this site is

primarily driven by overburden stress. Meanwhile, liquid water generated at the surface percolates into the firn and releases

latent heat when refreezing as ice lenses or ice layers, resulting in considerable variability in firn density. Due to relatively

low accumulation and high snowmelt rates at KAN_U, the firn density at this site is mainly influenced by liquid water and

135   remains generally high. Moreover, significant annual snowmelt events favour the formation of ice slabs at KAN_U,

impeding further liquid water infiltration at depth and facilitating liquid water runoff (MacFerrin et al., 2019). These two

sites are thus typical for assessing the capability of a firn densification model to simulate firn density under different

snowmelt rates and control mechanisms in the percolation zone.
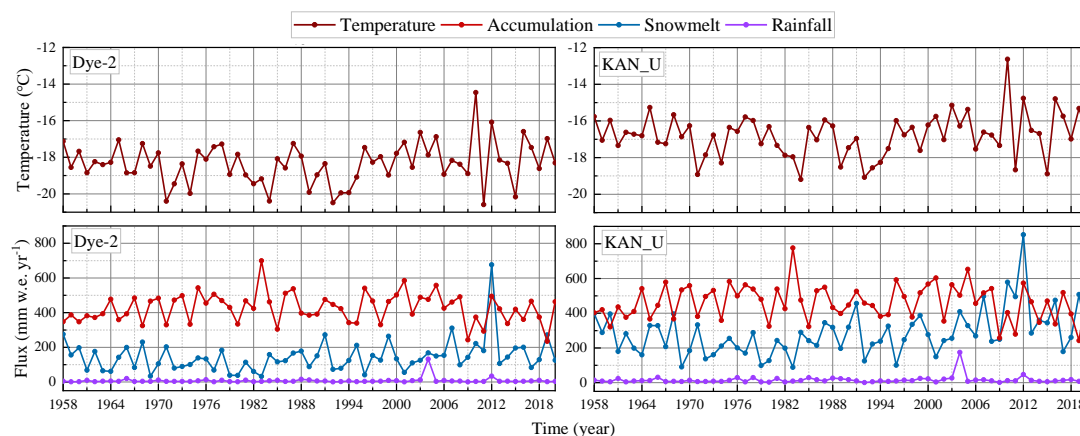
140

Figure 2. Time series of the annual mean surface temperature, annual accumulation, snowmelt and rainfall from RACMO2.3p2 at Dye-2 and KAN_U (1958-2020).

2.3 Firn cores

145 In order to validate the modelled firn density profiles, we compared the modelled results to punctual in situ measurements

obtained from firn cores. A set of 16 previously published cores with lengths exceeding 10 m in the study sites are collected

for this study (Table 2). These cores were primarily drilled in late April or May between 2012 and 2019 (Machguth et al.,

2016; MacFerrin et al., 2019; Vandecrux et al., 2019; Rennermalm et al., 2021), coinciding with substantial snowmelt, which

provided an optimal condition for observing firn density in the presence of liquid water. The naming of the cores follows the

150 same naming convention by Rennermalm et al. (2021), i.e., cores are labelled with the site name, drilling year and a

sequential number if more than one core was drilled in any year (e.g. KAN_U-12-1). All firn core records included data on

density and ice layer stratigraphy. The density of each core segment was same, and the stratigraphy of each core segment

was visually inspected at a vertical resolution of 0.01 m (Machguth et al., 2016; MacFerrin et al., 2019; Vandecrux et al.,

2019) or 0.005 m (Rennermalm et al., 2021). To estimate density profiles at the same frequency, we resample firn densities

155 to a resolution of 0.01 m. If density data for a specific core segment is absent, we assign it the mean density of the adjacent

two core segments. For density values measured from the cores exceeding 917 kg m^{-3} (the density of pure ice), we define

them as unreasonable (Rennermalm et al., 2021) and adjust them to 917 kg m^{-3}. Moreover, if the initial depth of firn core is

not zero (Dye-2-15, KAN_U-12-1, KAN_U-12-2, KAN_U-12-3, KAN_U-13-2, KAN_U-15, and KAN_U-17), the firn

densities preceding the initial depth are set to the mean surface density during 1958-2020, which is 315 and 320 kg m^{-3} for

160   Dye-2 and KAN_U respectively.

Table 2. Characteristics of firn cores used in this study, including core retrieval date, location information, elevation, initial and end depth below the surface, as well as source. Source refers to 1) Machguth et al., 2016, 2) MacFerrin et al., 2019, 3) Vandecrux et al., 2019, and 4) Rennermalm et al., 2021.

Core name	Date	Latitude (°)	Longitude (°)	Elevation (m a.s.l.)	Initial depth (m)	End depth (m)	Source
KAN_U-12-1	2012-05-01	67.00025	-47.02130	1840	0.80	10.68	1
KAN_U-12-2	2012-05-01	67.00025	-47.02138	1840	0.59	10.49	1
KAN_U-12-3	2012-05-01	66.99825	-47.02083	1840	0.17	10.26	1
KAN_U-13-1	2013-04-27	67.00025	-47.02263	1840	0	19.12	1
KAN_U-13-2	2013-04-28	66.99837	-47.02213	1840	0.79	15.94	1
KAN_U-15	2015-05-05	67.00042	-47.02472	1840	0.65	14.40	2
KAN_U-16	2016-04-28	67.00038	-47.02615	1838	0	16.51	2
KAN_U-17	2017-04-28	67.00025	-47.02263	1840	0.78	23.27	2
Dye-2-13-1	2013-05-05	66.47758	-46.28472	2119	0	16.64	1
Dye-2-13-2	2013-05-05	66.47260	-46.28298	2119	0	16.45	1
Dye-2-15	2015-05-21	66.47771	-46.28606	2126	0.81	19.27	3
Dye-2-16	2016-05-06	66.47260	-46.28298	2126	0	17.37	3
Dye-2-17-1	2017-05-11	66.47260	-46.28298	2126	0	22.97	3
Dye-2-17-2	2017-05-13	66.47804	-46.28713	2112	0	26.68	4
Dye-2-18	2018-05-09	66.47800	-46.28700	2112	0	19.78	4
Dye-2-19	2019-05-19	66.47800	-46.28900	2113	0	20.97	4

165   **3 Firn densification model**

After settling to the surface, fresh snow undergoes compaction under the forcing of overburden stress. Meanwhile, the liquid water composed from snowmelt and rainfall percolates downward into the firn column due to the porosity and permeability of the firn grains. Liquid water will refreeze and form ice lenses or ice layers when reaching a firn layer with sufficient cold content and pore space. Here, cold content refers to the energy required to raise the temperature of the firn to melting

170   temperature (Langen et al., 2017). Due to capillary forces, a portion of liquid water is retained within the firn layer, unable to percolate further or refreeze. In addition, once liquid water encounters an ice layer (between 0.1 and 1 m thick) or ice slab (thicker than 1 m), it is challenging to percolate further and thus departs from the firn column through runoff (Fig. 4a).

In order to simulate the firn density under the forcing of overburden stress and liquid water, we establish a 1D vertical

175   Lagrangian model with the vertically downward direction as the positive direction (Fig. 4b). The vertical coordinate, z, increases downwards. The base area of the firn column is defined as 1 m^2. The firn column is divided into a finite number of firn layers, each with a thickness denoted as dz, which is related to snow accumulation at each time step. This study sets time

step sizes as the time required for the snow accumulation to reach a specific value. Through continuous experimentation, the

optimal accumulation amount here is determined to be 0.014 m w.e. at Dye-2 and 0.017 m w.e. at KAN_U. New added

180 surface accumulation is instantly treated as the upper layer of the vertical firn column while removing one firn layer from the

bottom of the firn column. Every individual firn layer is partitioned into distinct contributions from firn, air, ice, and liquid

water, with each component expressed in terms of m w.e. units. Firn properties change from layer to layer due to the varying

proportions of these four components. Nevertheless, within each layer, firn properties are assumed to remain constant. We

keep track of the density of each firn layer during its downward motion to simulate the depth-density profile.

185
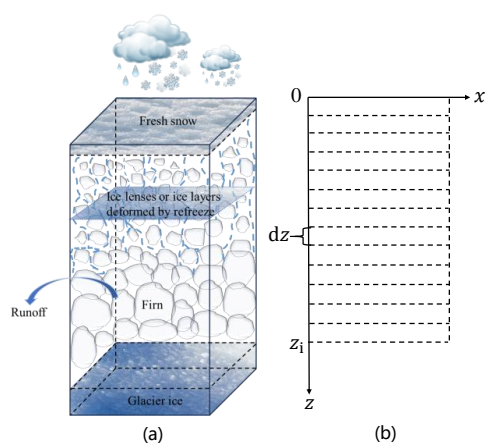
Figure 3. Schematic representation of firn densification processes (a) and simple layering scheme used in this study (b).

3.1 Fresh-snow density

190 An essential boundary condition for the model is the density of the first firn layer within the firn column, ρ_s (kg m^{-3}). Fresh-

snow density is typically stated as a constant value, like 350 kg m^{-3} (Stevens et al., 2020), or as a function of meteorological

variables such as temperature and wind speed (Keenan et al., 2021). Considering the dynamic nature of atmospheric

conditions, which leads to a certain variability in surface density, a parameterized equation may provide a more realistic

approximation of actual fresh-snow density than a constant value. Differing from earlier investigations, which typically use

195 the first 1.0 m of snow (Kuipers Munneke et al., 2015) and thus systematically overestimate the actual snow density at the

surface, Fausto et al. (2018) focused only on the upper 0.1 m of snow at 200 locations of the GrIS to develop a

parameterization for fresh-snow density and found:

$$\rho_s = 362.1 + 2.78 \cdot T_a, \tag{1}$$

Here, T_a is the annual mean near-surface (usually 2 m) air temperature (°C), ρ_s represents the fresh-snow density (kg m^{-3}).

200 This equation inherently involves densification from wind and drifting snow. Although the actual density of fresh snow could vary with each accumulation event, the parameterization is derived by fitting the measured snow densities to mean annual temperatures. Therefore, in this model, T_a is calculated as the average near-surface air temperature of the year preceding the accumulation event to avoid introducing an additional uncertainty.

3.2 Grain growth and microstructure evolution

205 The continuous accumulation of fresh snow subjects the underlying firn layer to augmented stress. Stress disparities develop at grain boundaries due to variations in grain boundary curvature and stored strain energy among crystal grains. High-stress regions on concave surfaces interacting with low-stress regions on other surfaces give rise to an unstable state, prompting grain boundary sliding and causing a rearrangement of grain structures. As a result, the system composed of grains undergoes motion aimed at minimizing surface area, leading to a gradual engulfing of smaller crystals by bigger ones, a

210 phenomenon usually known as grain growth (Ren et al., 2020).

The shape of firn grains is typically depicted as sphericity or dendricity. Considering the challenges associated with simulating dendritic grain growth and the lack of relevant laboratory observations and model simulations, we simulate firn grains as spherical grains. Grain growth is then simulated as a process of radius expansion around the grain's center. Hence,

215 the radius of a particle r (m) is determined from the initial radius r_0 (m) and the growth rate R_g (m^2 s^{-1}) as a function of time:

$$r^2(t) = R_g t + r_0^2, \tag{2}$$

The Arrhenius equation is used to calculate the growth rate R_g, which is a function of grain growth coefficient R_0 (m^2 s^{-1}), grain-growth activation energy E_g (kJ mol^{-1}), gas constant R (8.314 J (kg K)$^{-1}$), and firn temperature T (K):

$$R_g = R_0 \exp(-\frac{E_g}{RT}), \tag{3}$$

220 The above parameterization assumes linear grain growth under isothermal conditions. Research indicates that values of E_g vary between 47 kJ mol^{-1} (Gow, 1969) and 42.4 kJ mol^{-1} (Cuffey and Paterson, 2010). Following Arthern et al. (2010), we set R_0 to be 1.3×10^{-7} m^2 s^{-1} and E_g to be 42.4 kJ mol^{-1}. The initial grain radius, r_0, usually is prescribed as a constant value, such as 0.1 mm (Katsushima et al., 2009). In this study, we use the empirical formula obtained from Linow et al. (2012) to calculate the initial grain radius:

225 $$r_0\left(\bar{T}, \bar{b}\right) = b_0 + b_1 \bar{T} + b_2 \bar{b}, \tag{4}$$

with $b_0 = 0.781$ m, $b_1 = 0.0085$ m K^{-1}, $b_2 = -0.279$ yr (m w.e.)$^{-1}$, $\bar{T}$ is the mean annual temperature (K), and $\bar{b}$ is the mean annual accumulation rate (m w.e. yr^{-1}).

3.3 Firn temperature evolution

Following the CFM model, the vertical temperature distribution and its evolution are simulated by solving a one-dimensional

230   and time-dependent heat-transfer equation (Patankar, 1980):

$$\rho c_{\mathrm{f}} \frac{\partial T}{\partial t} = \frac{\mathrm{d}K}{\mathrm{d}z} \cdot \nabla T + K \cdot \nabla^2 T, \tag{5}$$

In this equation, K is the thermal conductivity of the firn (W m^{-1} K^{-1}), which is related to firn density ρ and firn temperature

T, thus $\frac{\mathrm{d}K}{\mathrm{d}z} = \frac{\partial K}{\partial \rho} \frac{\partial \rho}{\partial z} + \frac{\partial K}{\partial T} \frac{\partial T}{\partial z}$; c_{f} is the specific heat capacity of firn (J kg^{-1} K^{-1}), which is considered to be equal to the specific

heat capacity of ice here. Under one-dimensional conditions, $\nabla = \frac{\partial}{\partial z}$. Considering the effect of latent heat released during

235   refreezing, the firn temperature will be updated after liquid water refreezing (Sect. 3.5.3).

Firn thermal conductivity, a crucial factor in simulating heat diffusion, is extensively investigated based on field and

laboratory experiments (Van Dusen and Washburn, 1929; Schwerdtfeger, 1963; Yen, 1981; Sturm et al., 1997; Calonne et al.,

2011). Nevertheless, no universally accepted parameterization exists for firn thermal conductivity, and most of the existing

240   predictive formulas are developed for a given temperature or density range, making them inapplicable at temperatures or

densities outside of the provided range. Calonne et al. (2019) developed a parameterization of firn thermal conductivity from

3-D images of snow, firn, or porous ice microstructures, covering a density range from 100 to 888 kg m^{-3}, at different

temperatures. This parameterization has been confirmed to be valid for a wide range of temperatures and densities typically

observed in the firn layers of ice sheets, making it appropriate for simulations of the GrIS. Therefore, the firn thermal

245   conductivity follows Calonne et al. (2019) in this study.

3.4 Dry-firn compaction scheme

With the accumulation of new snow at the surface (the top of the firn column), the firn is buried deeper and tracked during

their downward motion. At every time step, each firn layer is compacted under the stress exerted by the gravity of snow/firn

250   above it. Therefore, firn properties are directly related to overburden stress, which causes sintering and mechanical creep and

is the dominant force in firn densification (van Kampenhout et al., 2017). The CROCUS model developed for mountain

snowpack (Brun et al., 1992, Vionnet et al., 2012) has been used to simulate firn densification on the GrIS (Langen et al.,

2017; Verjans et al., 2019). Verjans et al. (2019) indicated that incorporating a percolation scheme into a stress-based

densification model ensures that mass redistribution caused by percolation appropriately influences the densification process.

255   As in Verjans et al. (2019), we choose the CROCUS model as the dry-firn compaction scheme, which relates the overburden

stress σ (kg m^{-1} s^{-1}) to the densification rate with a viscosity η (kg s^{-1} m^{-1}):

$$\frac{\mathrm{d}\rho}{\mathrm{d}t} = \frac{\rho\sigma}{\eta}, \tag{6}$$

$$\eta = f_1 f_2 \eta_0 \frac{\rho}{c_\eta} \exp(a_\eta(T_\mathrm{m} - T) + b_\eta \rho), \tag{7}$$

where T_m is the melting temperature (273.15 K), $\eta_0 = 7.62237 \times 10^6$ kg s^{-1} m^{-1}, $a_\eta = 0.1$ K^{-1}, $b_\eta = 0.023$ m^3 kg^{-1}, $c_\eta = 358$

260   kg m^{-3} following van Kampenhout et al. (2017). f_1 and f_2 are two correction factors to snow viscosity that accounts for

viscosity differences due to the presence of liquid water and grain sizes respectively. Following Langen et al. (2017) and van

Kampenhout et al. (2017), f_2 is set to 4, neglecting the change in η for grain sizes smaller than 0.34 mm. f_1 is represented as

a function of the liquid water content θ_w (m^3 m^{-3}): $f_1 = 1/(1 + 60\theta_\mathrm{w})$.

3.5 Liquid water scheme

265   As long as liquid water is available at the surface and the porosity of the firn allows percolation, water will percolate to a

deeper layer by gravitation. Percolation proceeds until all the water is depleted or an impermeable layer is encountered,

where any excess water at that time step is instantly considered as runoff. For some firn layers, the pore space can

accommodate both air and water. The variable P (/) is used to denote the porosity of a firn layer with a thickness of dz,

which is defined as the ratio of the volume of pore space inside the firn layer to the total volume of the firn layer and

270   calculated from the firn density ρ and ice density ρ_i (917 kg m^{-3}): $P = 1 - \rho/\rho_\mathrm{i}$. The pore space within the firn layer,

denoted as φ (m^3), is determined by multiplying the porosity P by the thickness of the layer dz. Moreover, the vertical firn

water flux depends on the firn's irreducible water content (Coléou and Lesaffre, 1998), the firn's saturated (Calonne et al.,

2012) and unsaturated (Hirashima et al., 2010) hydraulic conductivities, and a coefficient that accounts for the effect of ice

content on the firn hydraulic conductivity (Colbeck, 1975). In this study, we use the Darcy-flow scheme in the CFM model

275   to simulate water percolation, capillary retention, and refreezing. A slight difference is that we calculate the water-holding

capacity according to Coléou and Lesaffre (1998) and calculate the irreducible water amount within each layer as the product

of that layer's liquid water volume and water-holding capacity.

3.5.1 Water saturation

The maximal pore space that can be occupied by liquid water is known as the saturated water volume. Considering the

280   volume expansion resulting from the refreezing of all liquid water within the pore space into ice, the saturated water content

is expressed as: $\theta_s = V_\mathrm{wm}/\mathrm{d}z$ (m^3 m^{-3}), where the saturated water volume $V_\mathrm{wm} = \varphi * (\rho_\mathrm{i}/\rho_\mathrm{w})$ (m^3). Due to the forcing of

capillary and adhesive forces, a small fraction of the water will be retained within some of the available pore space of the

firn layer and not subject to vertical transfer, often referred to as irreducible water. The maximum water saturation that can

be sustained by the capillary tension of firn grains is termed the water-holding capacity, S_{wi} (/), with values employed in

285 models varying widely (Langen et al., 2017). For example, a common practice is to use constant values (Colbeck, 1974;

Yamaguchi et al., 2010; Reijmer et al., 2012; Steger et al., 2017). In this study, we follow the formulation from Coléou and

Lesaffre (1998), where the water-holding capacity S_{wi} is taken as a function of firn density ρ:

$$S_{wi} = \frac{W_{mi}}{1-W_{mi}} \frac{\rho_i \rho}{\rho_w(\rho_i - \rho)},$$ (8)

$$W_{mi} = 0.057 \frac{\rho_i - \rho}{\rho} + 0.017,$$ (9)

290 Assuming the liquid water volume within one firn layer is V_w (m^3), the irreducible water content θ_i (m^3 m^{-3}) can be

represented as $\theta_i = V_{wi}/dz$, with $V_{wi} = V_w * S_{wi}$ (m^3). The effective water saturation Θ (/) can be expressed as

$$\Theta = \frac{\theta_w - \theta_i}{\theta_s - \theta_i},$$ (10)

where $\theta_i < \theta_w < \theta_s$, the liquid water content θ_w is given as the ratio of V_w to dz. Here, at each time step, the liquid water

volume in the j-th firn layer, $(V_w)_j$, is calculated as

295 $(V_w)_j = (V'_w)_j + \min(V_{tot} - \sum_{n=1}^{j-1}(V_w)_n, \ (V_{wm})_j - (V'_w)_j),$ (11)

where V'_w represents the liquid water volume from the preceding time step that can be refrozen but has not yet refrozen due to

the limited cold content, V_{tot} is the total liquid water input during this time step, $(V_{wm} - V'_w)$ represents the maximum

amount of liquid water that can be accommodated in a firn layer (including irreducible water). When encountering an

impermeable firn layer, all excess liquid water runoff and the liquid water volume below this layer is equal to its value at the

300 preceding time step.

3.5.2 liquid water amount within each layer

Water in excess of the irreducible water volume is allowed to move downward, we define the liquid water volume available

for flow within a firn layer to be V_{av} (m w.e.), i.e.: $V_{av} = V_w - V_{wi}$. Because firn is a porous material, water flow in the firn

column can be estimated using Darcy's law. Water flux q (m s^{-1}) is a function of hydraulic conductivity K_w (m s^{-1}) and

305 capillary suction h (m):

$$q = K_w(\frac{dh}{dz} + 1),$$ (12)

Here, dh/dz is the vertical hydraulic gradient in capillary suction, and the second term $(+1)$ represents gravity. Porosity and

pore structures influence capillary suction and hydraulic conductivity. However, characterizations such as pore shape, pore

connectivity, and tortuosity are difficult to measure or simulate directly. In this study, following Hirashima et al. (2010) and

310 Langen et al. (2017), the hydraulic conductivity and the capillary suction are parameterized in terms of firn grain radius r,

effective liquid saturation Θ, and firn density ρ. Shimizu (1970) formulated a saturated hydraulic conductivity based on laboratory experiments using kerosene, showing that hydraulic conductivity can be estimated as a function of grain size and snow density:

$$K_s = 0.308 \frac{g}{\nu_w} r^2 \exp(-0.0078\rho),\tag{13}$$

315   Here, g is the acceleration due to gravity ($m \cdot s^{-2}$), and $\nu_w = 1.787 \times 10^{-6}$ m^2 s^{-1} is the kinematic viscosity of water. Van Genuchten (1980) developed an accurate expression for the capillary suction in soil, and Hirashima et al. (2010) further optimized the expression:

$$h = \frac{1}{\alpha}(\Theta^{-\frac{1}{m}} - 1)^{\frac{1}{n}},\tag{14}$$

In this equation, $\alpha = 14.6r + 1.9$, $n = 15.68\exp(-0.92r) + 1$, $m = 1 - \frac{1}{n}$. Van Genuchten (1980) combined the theory of

320   Mualem (1976) to estimate the unsaturated hydraulic conductivity, K_r, as follows:

$$K_r = \Theta^{\frac{1}{2}}[1 - (1 - \Theta^{\frac{1}{m}})^m]^2,\tag{15}$$

The hydraulic conductivity of firn can be expressed as the multiplication of the saturated hydraulic conductivity K_s, and the unsaturated hydraulic conductivity K_r. Furthermore, the ice lenses or ice layers formed by refreezing have the potential to impede the infiltration of liquid water. This effect is parameterized by introducing an additional permeability factor K_f,

325   resulting in the equation $K_w = K_s * K_r * K_f$. In order to make the model more sensitive to the formation of thin ice lenses and to reduce excessive refreezing, we set a thick of 0.1 m as the impermeable threshold, which is the maximum thickness of ice lenses. Therefore, K_f is set to zero when the ice thickness is less than 0.1 m, otherwise $K_f = 1$.

Based on the above information, we can calculate the water transport amount within a Darcy time step, usually denoted as

330   $q\mathrm{d}\tau$. Hirashima et al. (2010) suggested that the simulations will become unstable if the water transport amount in a Darcy time step approaches the water content. Thus, the Darcy time steps must be appropriately selected. They pointed out that the limit of the water transport amount in a Darcy time step, $q_{\lim}$ (m w.e.), is approximated by the amount needed to reach equilibrium conditions between two adjacent vertical layers. Following the CFM model, we initially assume a value of 60 seconds for $\mathrm{d}\tau$ and subsequently iteratively adjust this value to approximate the time required for achieving equilibrium

335   conditions (Equation 20 in Hirashima et al. (2010)). Finally, the water transport amount in a Darcy time step is calculated as $q_{\lim}[1 - \exp(-\frac{q}{q_{\lim}}\mathrm{d}\tau)]$ (m w.e. units). Considering the liquid water volume available for flow, the actual water transport amount in a firn layer is the minimal value between $q_{\lim}[1 - \exp(-\frac{q}{q_{\lim}}\mathrm{d}\tau)]$ and V_{av}, and we denote it using u. The inflow into the j-th firn layer is the outflow from the (j-1)-th firn layer. Therefore, the liquid water volume within j-th layer is

updated as $(V_w)_j + u_{j-1} - u_j - R_j$, where V_w is the liquid water volume before water flow, calculated by Eq. (11); R_j

340   represents the liquid water loss through lateral runoff in j-th firn layer calculated by the Darcy parameterization.

3.5.3 Refreezing

The increased mass of a given firn layer caused by refreezing is calculated according to its maximum refreezing potential, C_r

(kg), and the liquid water amount available for refreezing, V_w (m w.e.), within the firn layer:

$$m_r = \min(C_r, \ V_w * \rho_w), \tag{16}$$

345   Given the specific heat capacity of ice, $c_i = 152.5 + 7.122T$ (Cuffey and Paterson, 2010), and the latent heat of fusion, $\mathcal{L}$

(3.335×10^5 J kg^{-1}), the maximum refreezing potential can be defined as

$$C_r = \frac{Q_{cold}}{\mathcal{L}} = \frac{c_i * m * (T_m - T)}{\mathcal{L}}, \tag{17}$$

where Q_{cold} is the cold content of the firn layer, m is the mass of the firn layer before refreezing. Considering the latent heat

released by refreezing, which can be calculated as: $Q_L = m_r * \mathcal{L}$, the firn temperature is updated to

350    $$T = T_m - \frac{Q_{cold} - Q_L}{c_i(m + m_r)}, \tag{18}$$

Finally, the firn density in each firn layer with the presence of liquid water may be calculated as $\rho = (m + m_r)/dz$.

3.6 Model Initialization

The initial model density, temperature, grain size, and liquid water content in the firn column are obtained by repeatedly

applying the spin-up period 1958-1979, which is considered representative of the climate of the preceding few hundred years

355   and during which the forcing (i.e. surface accumulation, liquid water flux, and skin temperature) is assumed to have

remained reasonably constant (van den Broeke et al., 2009; Brils et al., 2022). Observations and model studies support the

assumption that the Greenland climate and surface mass balance (SMB) started to change significantly in the 1990s

(Enderlin et al., 2014; McMillan et al., 2016), confirming that the period 1958-1979 can be selected for initialization

purposes. Initialization is considered complete until the firn layer is in equilibrium with the surface climate. The equilibrium

360   is roughly reached when the entire firn column (defined here as the depth where the density reaches the pore close-off

density of 830 kg m^{-3}) has been fully refreshed by accumulation (Veldhuijsen et al., 2023). Due to variable snow

accumulation rates, the required spin-up time can vary significantly, resulting in a self-adaptive time frame where the 22-year

climate interval is repeated to provide a time series long enough for a full firn column refreshment. If the spin-up time

required is not divisible by 22, we round up to the next integer to exceed the required time.

3.7 Metrics of model evaluation

Several metrics are used to compare the modelled firn density to both the observations and the previous firn density modelling studies. The root mean square error (RMSE) is a statistical measure used to assess the accuracy of a model's simulations compared to observations. A lower RMSE value indicates better agreement between simulations and observations, implying higher accuracy of the model. The formula for RMSE is

$$\text{RMSE} = \sqrt{\frac{\sum_{i=1}^{n}(M_i - O_i)^2}{n}}, \tag{19}$$

where M_i is the modelled value, O_i is the observed value, and i iterates over n number of values. To quantify the goodness of fit of model simulations, we use the Nash-Sutcliffe efficiency coefficient (NSE), which is typically employed in hydrological modelling (Nash and Sutcliffe, 1970). The value of NSE ranges from negative infinity to 1, with values closer to 1 indicating superior simulation accuracy. A value of 1 indicates perfect model performance and a value of 0 suggests that the simulated results align with the mean level of the observed values. It is calculated as:

$$\text{NSE} = 1 - \frac{\sum_{i=1}^{n}(O_i - M_i)^2}{\sum_{i=1}^{n}(O_i - \bar{O})^2}, \tag{20}$$

where $\bar{O}$ is the mean of observations. Moreover, we use the correlation coefficient (r) to quantify the relationship between observations and simulations. In order to estimate the overall capability of the model to reproduce density profiles and the extent to which the model underestimates or overestimates, we calculate the relative bias between observed and modelled firn density and FAC. The relative bias in firn density is calculated as

$$\text{Relative bias} = \frac{\sum_{i=1}^{n}(M_i - O_i)}{\sum_{i=1}^{n}(O_i)} \times 100\%, \tag{21}$$

The FAC is the integrated volume of air contained within the firn from the surface to a certain depth per unit area (van Angelen et al., 2013; Ligtenberg et al., 2018), which is represented as

$$\text{FAC} = \int_{0}^{z_m} \frac{\rho_i - \rho(z)}{\rho_i} \, dz, \tag{22}$$

where z_m is the maximal observation depth, $\rho(z)$ is the firn density at a given depth. For comparison, we resample the observed and simulated density to a resolution of 0.01 m, so dz = 0.01 here.

4 Results

4.1 Dye-2

Based on the initial firn depth-density profile obtained from the spin-up procedure, we run the established firn densification model to calculate the firn density for each firn layer at each time step between 1958 and 2020. To qualitatively assess the accuracy of the firn densification model in forming a depth-density profile, we compare the modelled firn density with the observed density profile and ice layer stratigraphy from the core of the closest date (Fig. 4). Compared to the dry-firn density

profile, the modelled firn density increases sharply for all 8 cores, especially in the top 10 m of the firn column. This result can be attributed to the increased snowmelt in recent years and the subsequent refreezing within the firn layer, which forms

395 ice lenses and/or ice layers. Due to the high snowmelt rate in 2012, a meter-thick ice layer formed and was later buried in the following months and years, emerging at approximately 5 m depth in the Dye-2-19 core. Below this ice layer, several thin ice lenses and density variability are exhibited as a result of seasonal and interannual variations in snowmelt. Compared to observations, the model partly simulates the high-density firn layers observed in the first 10 m of the firn column while underestimating the density variability observed.

400
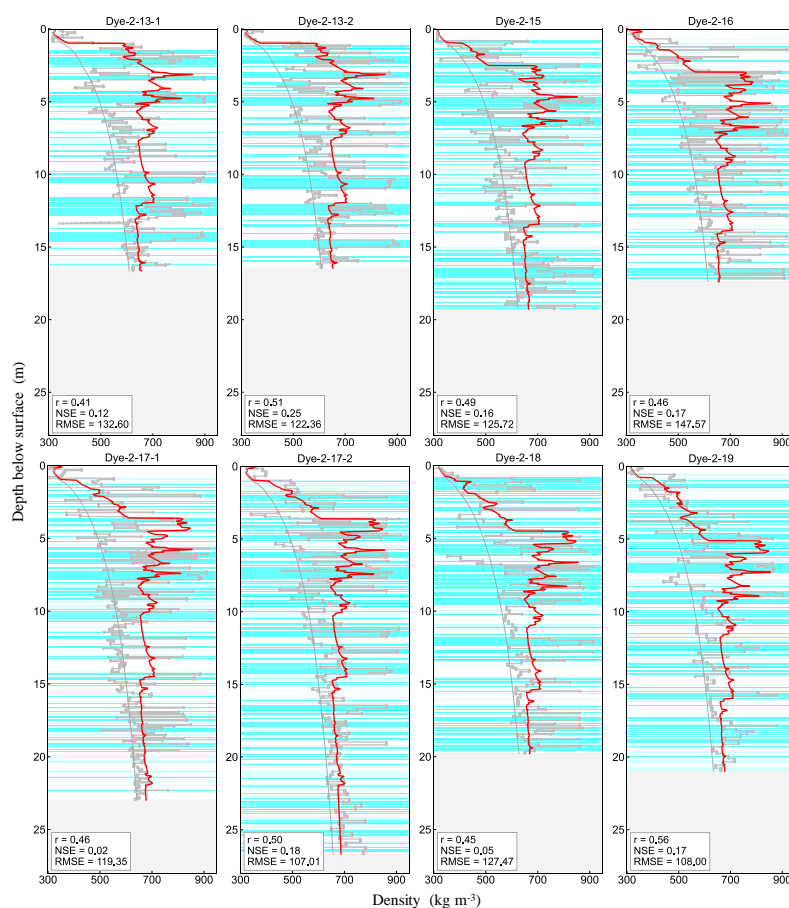
Figure 4. Observed (gray dotted line) and modelled (red solid line) firn depth-density profiles at Dye-2. Ice layer stratigraphy is shown as cyan horizontal lines. The gray-shaded regions indicate no data. The thin inclined line denotes the dry firn density simulated using the CROCUS model. The correlation coefficient (r), Nash-Sutcliffe efficiency coefficient (NSE), and root mean

405 **square error (RMSE) are displayed in the bottom left of each panel.**

To quantify the model's performance in reproducing the heterogeneity of firn density, we employed three evaluation metrics: r, NSE, and RMSE. Additionally, the relative bias in firn density and FAC are calculated to understand the overall capability of the model in reproducing density profiles and the extent to which the model underestimates or overestimates (Table 3). In

410 general, the simulations align with the average level of observations, with the relative bias in density ranging from 0.36% (Dye-2-13-2) to 6% (Dye-2-17-1), and the smallest NSE being 0.02 (Dye-2-17-1). Moreover, the correlation coefficient (r) is around 0.5 for all cores, also indicating that the model is able to capture the general trend of observations at Dye-2 to some extent, but it does not accurately reproduce the specific characteristics of the observed density. The Dye-2-16 core exhibits the largest process error (RMSE=147.57 kg m^{-3}) among all 8 cores, likely due to the greatest density variability in this core.

415 However, the relative bias in density and FAC of this core is not the highest, possibly due to the model's overestimations and underestimations of the observed density counterbalancing each other. The Dye-2-17-2 core exhibits the highest relative bias in density (6%) among 8 cores. This may be attributed to the dry-firn density, which is theoretically expected to closely match the low-density peaks in the observed density profiles, being overestimated in this core.

420 **Table 3. Statistics and model outputs of 8 firn cores drilled at Dye-2 between 2013 and 2019, including the mean observed and modelled firn density for the entire core depth range ($\bar{\rho}_O$ and $\bar{\rho}_M$), relative bias in density, observed and modelled FAC and their relative bias.**

Core name	$\bar{\rho}_O$ (kg m^{-3})	$\bar{\rho}_M$ (kg m^{-3})	Relative bias in density (%)	Observed FAC (m)	Modelled FAC (m)	Relative bias in FAC (%)
Dye-2-13-1	630.68	645.38	2.33	5.20	4.93	-5.13
Dye-2-13-2	642.98	645.32	0.36	4.92	4.87	-0.85
Dye-2-15	616.34	641.28	4.05	6.32	5.79	-8.29
Dye-2-16	629.60	644.75	2.41	5.44	5.16	-5.27
Dye-2-17-1	615.72	652.66	6.00	7.55	6.62	-12.26
Dye-2-17-2	646.11	656.76	1.65	7.88	7.57	-3.93
Dye-2-18	625.25	640.99	2.52	6.29	5.95	-5.40
Dye-2-19	615.12	642.36	4.43	6.90	6.28	-9.02

4.2 KAN_U

425 Characterized by warm climatic conditions and abundant snowmelt, the modelled firn density generally remains high at KAN_U (Fig. 5). For the KAN_U-13-1 and KAN_U-13-2 cores, many high-density firn layers are observed within the 1-4 m depth range of the firn column, which is primarily attributed to high snowmelt rates in 2010, 2011, and 2012, as well as the subsequent refreezing. These high-density layers form an approximately three-meter-thick ice slab, which becomes buried downward in the following months and years. In the observations, an almost continuous ice slab is observed in the

430 upper of all cores, with varying thicknesses among the cores. Taking the KAN_U-13-1 core as an example, the model

reproduces the high-density layers at 1-4 m depth. In the approximately 4-6 m depth range, the firn density is slightly

underestimated, possibly related to the percolation scheme of matrix flow. The matrix flow typically remains constrained to

the upper several meters of the firn column and cannot transfer water below ice layers (Verjans et al., 2019). As a result,

during the high-snowmelt summers from 2010 to 2012, liquid water leaves the firn column through runoff after encountering

435 ice layers. However, in reality, in sites like KAN_U where liquid water is abundant, preferential flow is likely to bypass ice

layers and thus refreeze the cold underlying firn layers, resulting in thicker ice slabs than simulations.
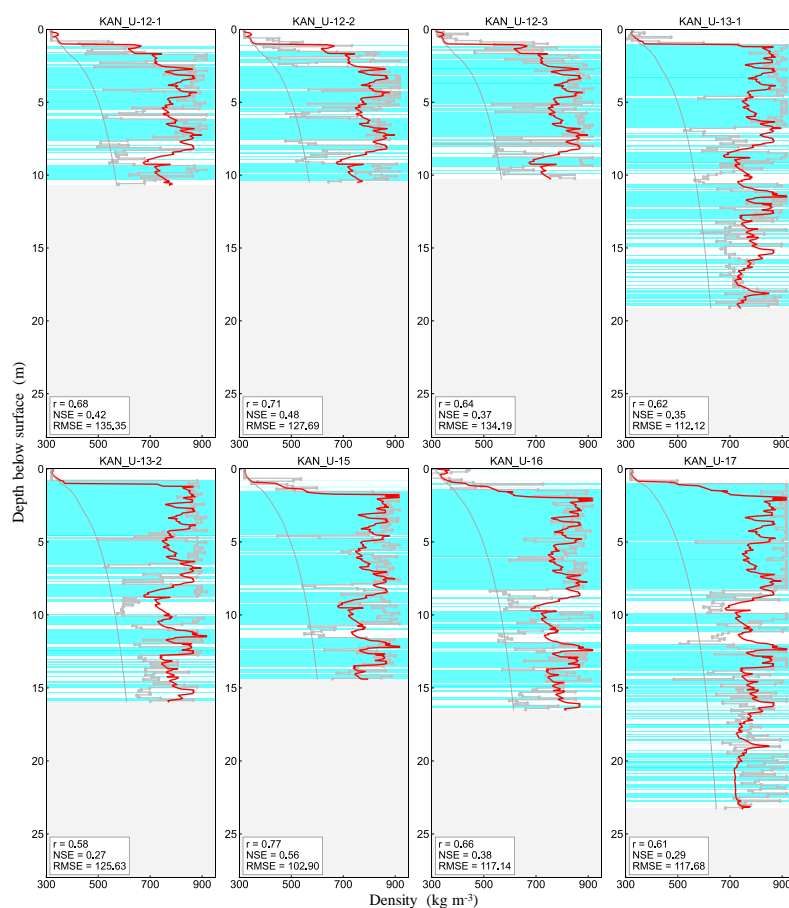
Figure 5. Observed (gray dotted line) and modelled (red solid line) firn depth-density profiles at KAN_U. Ice layer stratigraphy is

440 **shown as cyan horizontal lines. The gray-shaded regions indicate no data. The thin inclined line denotes dry firn density simulated**

using the CROCUS model. The correlation coefficient (r), Nash-Sutcliffe efficiency coefficient (NSE), and root mean square error

(RMSE) are displayed in the bottom left of each panel.

The modelled depth-density profiles compare well within uncertainties to observations for all cores, primarily due to the

445 model capturing the high-density layers and partly reproducing the presence of ice slabs. The relative deviation in density is

within ±5%, and NSE ranges from 0.27 (KAN_U-13-2) to 0.56 (KAN_U-15). However, the model is unable to accurately simulate low-density firn layers that are either unaffected or minimally affected by liquid water, despite the fact that these low-density layers are few at KAN_U. As a result, the model demonstrates the best performance in the KAN_U-15 core (r=0.77, NSE = 0.56, and RMSE = 102.90 kg m^{-3}), which has the fewest low-density firn layers among all 8 cores. The

450 KAN_U-17 core exhibits the largest density bias (-4.71%) and FAC bias (30.96%) among all cores, possibly associated with underestimated density within the 1-8 m depth range. In this range, numerous observed density values are deemed unreasonable (exceeding 917 kg m^{-3}), and we set these values to 917 kg m^{-3}.

Table 4. Statistics and model outputs of 8 firn cores drilled at KAN_U between 2012 and 2017, including the mean observed and

455 **modelled firn density for the entire core depth range ($\bar{\rho}_O$ and $\bar{\rho}_M$), relative bias in density, observed and modelled FAC and their relative bias.**

Core name	$\bar{\rho}_O$ (kg m^{-3})	$\bar{\rho}_M$ (kg m^{-3})	Relative bias in density (%)	Observed FAC (m)	Modelled FAC (m)	Relative bias in FAC (%)
KAN_U-12-1	705.15	733.06	3.96	2.47	2.14	-13.18
KAN_U-12-2	714.41	732.29	2.50	2.32	2.11	-8.82
KAN_U-12-3	738.78	731.58	-0.98	1.99	2.07	4.04
KAN_U-13-1	766.33	766.11	-0.03	3.14	3.15	0.14
KAN_U-13-2	766.24	768.40	0.28	2.62	2.58	-1.43
KAN_U-15	771.56	752.97	-2.41	2.28	2.58	12.79
KAN_U-16	742.03	759.12	2.30	3.15	2.84	-9.77
KAN_U-17	796.00	758.54	-4.71	3.07	4.02	30.96

5 Discussion

5.1 Comparison with previous studies

460 In this section, we compare the simulation results obtained at Dye-2 and KAN_U with previous firn density modelling studies at these two sites by qualitatively and/or quantitatively comparing them with firn density observations, respectively. Specifically, the modelled firn density at Dye-2 provided by Vandecrux et al. (2020c) and the modelled FAC at KAN_U provided by Verjans et al. (2019) are compared to our simulations. Here, the Dye-2-13-2 core is selected for mutual comparison of the models by considering the principle of selecting a longer core to compare more information and choosing

465 a core with fewer outliers within the available time ranges. Nine firn densification models used in Vandecrux et al. (2020c) are listed in Table 5. To compare the modelled firn density of each model with the observations from the Dye-2-13-2 core, we select the simulated depth-density profiles corresponding to midnight on the core drilling date from the outputs of the nine models and then resample them to a vertical resolution of 0.01m. The modelled firn density in the KAN_U-13-1 core is

selected to calculate the top 15 m FAC, which is then compared with the FAC results simulated using different densification

470   schemes in this core by Verjans et al. (2019). We refer the reader to Verjans et al. (2019) for the modelled density profiles of

different densification schemes and more details on the parameterization of different densification schemes.

Table 5. List of firn densification models used for comparison at Dye-2, including the dry-firn densification scheme and water flow scheme used in each model. The model abbreviation is consistent with the model code name in Vandecrux et al., 2020c.

Model abbreviation	Dry-firn densification scheme	Water flow scheme	Reference
CFMCr	CROCUS (Vionnet et al., 2012)	Deep percolation	Stevens et al. (2020)
CFMKM	KM (Kuipers Munneke et al., 2015)	Deep percolation	Verjans et al. (2019)
DMIHH	CROCUS (Vionnet et al., 2012)	Darcy's law	Langen et al. (2017)
DTU	SIM (Sørensen et al., 2011; Simonsen et al., 2013)	Bucket scheme	Sørensen et al. (2011); Simonsen et al. (2013)
GEUS	CROCUS (Vionnet et al., 2012)	Darcy's law	Vandecrux et al. (2018, 2020a)
IMAUFDM	KM (Kuipers Munneke et al., 2015)	Bucket scheme	Ligtenberg et al. (2011, 2018); Kuipers Munneke et al. (2015)
MeyerHewitt	HL (Herron and Langway, 1980)	Darcy's law	Meyer and Hewitt (2017)
UppsalaUniBucket	LIG (Ligtenberg et al., 2011)	Bucket scheme	Van Pelt et al. (2012, 2019)
UppsalaUniDeepPerc	LIG (Ligtenberg et al., 2011)	Deep percolation	Marchenko et al. (2017)
This study	CROCUS (Vionnet et al., 2012)	Darcy's law	--

475
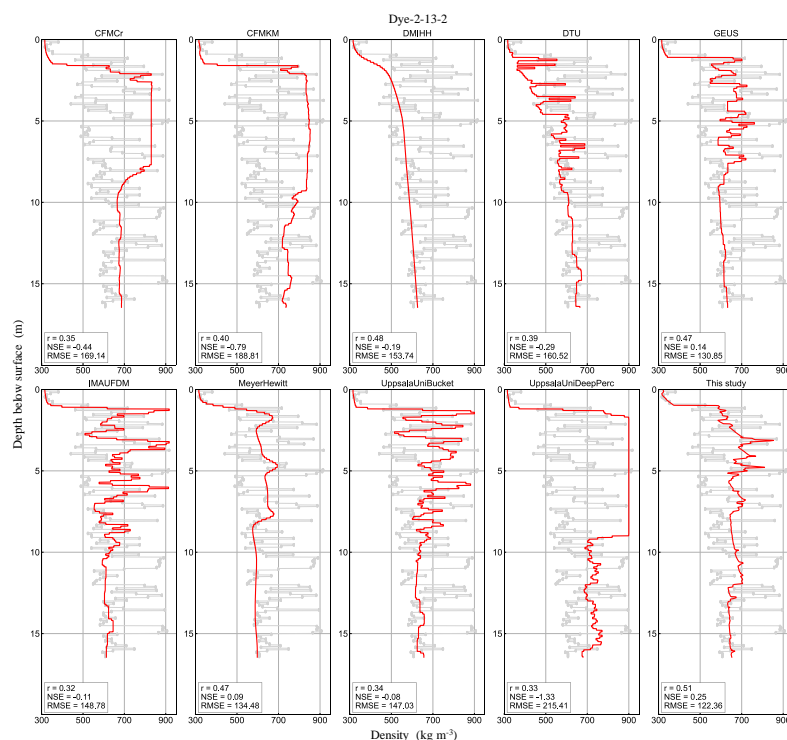
Figure 6. Observed (gray dotted line) and modelled (red solid line) firn depth-density profiles at the Dye-2-13-2 core.

At the Dye-2-13-2 core, compared to the other nine models, the model in this study exhibits the smallest relative bias in

480   density (0.36%) and FAC (-0.85%), as well as the highest accuracy, with the lowest RMSE of 122.36 kg m^{-3} and the highest

NSE of 0.25 (Fig. 6 and Table 6). The CFMCr, CFMKM, and UppsalaUniDeepPerc models build up an ice slab of several

meters thick near the surface, where no such ice slabs are observed, possibly attributed to the fact that these three models

consider both matrix flow and preferential flow. Preferential flow pathways enable water to bypass ice layers and refreeze

within the cold underlying firn, resulting in an overestimation of firn density at the minimal snowmelt production site of

485   Dye-2 (with the relative density bias of 8.57%, 16.40%, and 20.55%, respectively). The sharp contrasts between low-density

layers and high-density layers are smoothed in the DMIHH and MeyerHewitt models, which follow an Eulerian framework.

Using the matrix flow scheme (bucket-type percolation scheme or Darcy-flow scheme), as well as a Lagrangian framework,

the DTU, GEUS, IMAUFDM, UppsalaUniBucket, and our models all simulate thin, high-density layers formed by

refreezing. The DTU model only allows water retention and refreezing in the top firn layer, thus underestimating the overall

490   firn density (-12.72%). The GEUS model underestimates the firn density below 9 m (-5.67%). The IMAUFDM and

UppsalaUniBucket models exhibit density variability within the top 10 m, with overestimation of firn density at certain

depths, resulting in large RMSE values (148.78 kg m^{-3} and 147.03 kg m^{-3}, respectively).

Table 6. Statistics and model outputs of firn density profiles simulated by 10 firn densification models at Dye-2-13-2, including the

495   **mean firn density and FAC for the entire core depth range, relative bias in density and FAC. A slash indicates no data.**

Model	Mean density (kg m^{-3})	Relative bias in density (%)	FAC (m)	Relative bias in FAC (%)
Observation	642.98	/	4.92	/
This study	645.32	0.36	4.87	-0.85
CFMCr	698.09	8.57	3.93	-20.11
CFMKM	748.44	16.40	3.02	-38.49
DMIHH	552.66	-14.05	6.54	32.96
DTU	561.21	-12.72	6.38	29.84
GEUS	606.50	-5.67	5.57	13.31
IMAUFDM	626.91	-2.50	5.20	5.87
MeyerHewitt	592.93	-7.79	5.81	18.27
UppsalaUniBucket	645.69	0.42	4.87	-0.99
UppsalaUniDeepPerc	775.09	20.55	2.55	-48.21

At the KAN_U-13-1 core, the simulated top 15 m FAC in this study aligns well with the observed FAC in the top 15 m, with

a relative bias of 1.22% (Table 7), indicating that the model successfully captures the overall characteristics of the upper firn

density. In the density profile of the KAN_U-13-1 core, an almost continuous ice slab is observed over the 1-7 m depth range

500 (Fig. 5 in this study and Fig. 8 in Verjans et al. (2019)). Below this ice slab, the firn density becomes more variable but

remains generally high. In this study, the modelled density in the top 4 m closely aligns with the observed density,

reproducing the presence of the ice slab observed (Fig. 5). Additionally, the model captures the high-density layers around

11-14 m depth. All three percolation schemes in Verjans et al. (2019) do not capture the high-density firn layers caused by

the formation of ice slabs, with the modelled maximum density reaching approximately 830 kg m^{-3} (Fig. 8 in Verjans et al.

505 (2019)). The BK and R1M schemes significantly overestimate the top 15 m FAC (59.35% and 50%), which implies a

significant underestimation of firn density, likely due to the matrix flow being unable to percolate liquid water to deeper

depths and thus underestimating refreezing. The top 15 m FAC of the DPM scheme closely matches the observation (-

2.44%). However, the DPM density profile exhibits a nearly constant density value within the depth range of 3 to 17 m,

approximately 810 kg m^{-3}, not reproducing the density fluctuations between high-density layers and low-density layers

510 observed.

Table 7. The top 15 m FAC and its relative bias with observation at the KAN_U-13-1 core, which is both studied in Verjans et al. (2019) and this study. Verjans et al. (2019) implemented three types of water percolation schemes: the so-called bucket approach (BK), the Richards equation (Richards, 1931) in a single domain (R1M), and the Richards equation in a dual domain (DPM).

515 **Among three percolation schemes, the BK and R1M schemes only consider matrix flow, while the DPM scheme accounts for both matrix flow and preferential flow. We refer to Verjans et al. (2019) more details on different densification schemes. A slash indicates no data.**

Model	Top 15 m FAC (m)	Relative bias with observed FAC (%)
Observation	2.46	/
This study	2.49	1.22
CROCUS BK wh02 ip810	3.92	59.35
CROCUS R1M grLK ip810	3.69	50.00
CROCUS DPM grLK ip810	2.40	-2.44

5.2 Comparison of different dry-firn densification schemes

520 To investigate differences in the depth-density profiles caused by different dry-firn densification schemes, we conducted

simulations using five dry-firn densification schemes listed in Table 5, which are CROCUS, HL, KM, LIG, and SIM. Except

for the dry-firn densification schemes, the model configurations and climatic forcing for all five models are identical. We

select the longest two firn cores at two sites (Dye-2-17-2 and KAN_U-13-1, respectively) to compare the simulated firn

density with observations. Note that KAN_U-17 is the longest core at KAN_U, but it is not selected due to the high number

525 of outliers (density greater than 917 kg m^{-3}) at this core.

The stress-based CROCUS model exhibits the closest mean density (1.65% at Dye-2, and -0.03% at KAN_U) and FAC (-3.93% at Dye-2, and 0.14% at KAN_U) to observations than the other four accumulation-rate-based models (HL, KM, LIG, SIM). This is possibly attributed to the stress-based nature of the CROCUS model ensuring appropriate mass redistribution

530   related to percolation, which affects densification (Verjans et al., 2019). The density profile simulated by the HL model is generally similar to that of the CROCUS model and exhibits more density variability. In contrast, the CROCUS model shows closer agreement with observations below 12 m depth at KAN_U. The constitutive equations of the KM, LIG, and SIM models are all based on Arthern et al. (2010), resulting in relatively similar simulation results for these three models at both Dye-2 and KAN_U. Compared to the CROCUS and HL models, these three models exhibit more sensitivity to temperature,

535   resulting in an overestimation of firn density, particularly below 15 m depth. Among them, the SIM model demonstrates the most pronounced overestimation, causing the highest mean density (11.13% at Dye-2, and 8.54% at KAN_U) and the smallest FAC (-26.55% at Dye-2, and -43.44% at KAN_U).
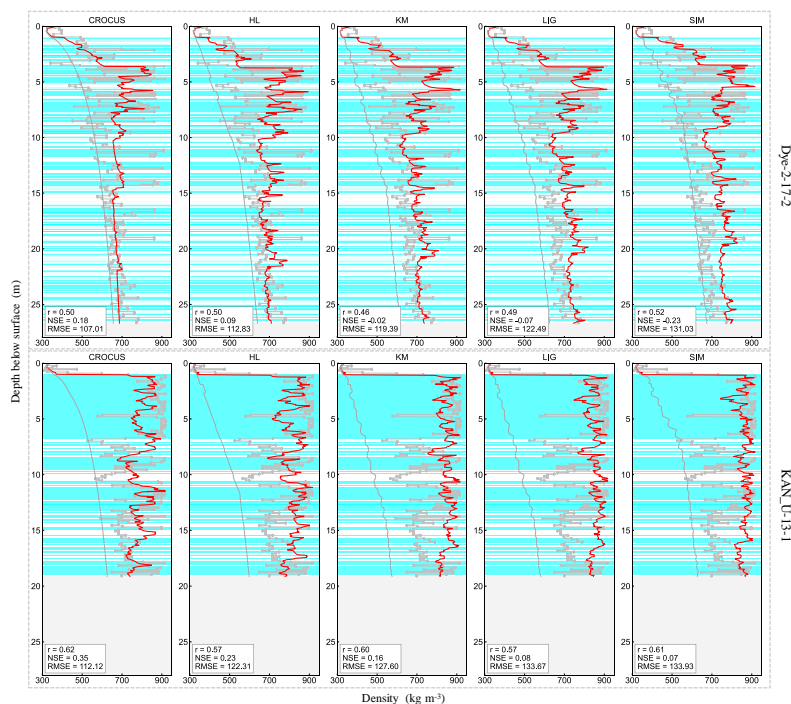
540   **Figure 8. Observed (gray dotted line) and modelled (red solid line) firn depth-density profiles at the Dye-2-17-2 and KAN_U-13-1 cores. The modelled density profiles are driven by different dry-firn densification schemes. Ice layer stratigraphy is shown as cyan horizontal lines. The gray-shaded regions indicate no data. The thin inclined line denotes dry firn density simulated using the corresponding dry-firn densification models. The correlation coefficient (r), Nash-Sutcliffe efficiency coefficient (NSE), and root mean square error (RMSE) are displayed in the bottom left of each panel.**

545

Table 8. Statistics and model outputs of firn density profiles at the Dye-2-17-2 and KAN_U-13-1 cores, including the mean firn density and FAC for the entire core depth range, relative bias in density and FAC. A slash indicates no data.

Core name	Model	Mean density (kg m⁻³)	Relative bias in density (%)	FAC (m)	Relative bias in FAC (%)
	Observation	646.11	/	7.88	/
	CROCUS	656.76	1.65	7.57	-3.93
Dye-2-17-2	HL	667.53	3.32	7.26	-7.91
	KM	677.98	4.93	6.95	-11.76
	LIG	691.45	7.02	6.56	-16.74
	SIM	718.03	11.13	5.79	-26.55
	Observation	766.33	/	3.14	/
	CROCUS	766.11	-0.03	3.15	0.14
KAN_U-13-1	HL	788.38	2.88	2.68	-14.64
	KM	816.99	6.61	2.09	-33.62
	LIG	820.76	7.10	2.01	-36.13
	SIM	831.77	8.54	1.78	-43.44

5.3 Comparison of different water flow schemes

550   Besides the dry-firn densification scheme, the choice of water flow scheme is also a crucial step in modelling firn density in the percolation zone. Verjans et al. (2019) demonstrated that apart from considering preferential flow, differences in the depth-density profiles simulated by schemes only employing matrix flow are minimal. In this section, we compare the depth-density profiles simulated using three different matrix flow schemes: the water flow scheme in Sect. 3.5, the Darcy-flow scheme, and the bucket percolation scheme. The latter two flow schemes are directly obtained from the CFM model and

555   share the same model configurations as the scheme in this study. Consistent with Sect. 5.2, the Dye-2-17-2 and KAN_U-13-1 cores are selected to compare the firn depth-density profiles simulated by the three flow schemes with observations.

All three schemes are demonstrated to have the ability to reproduce the bulk density condition of the firn column at both Dye-2 and KAN_U, with a maximum relative bias of 2.64% (Table 9). Among three percolation schemes, the scheme used in

560   this study exhibits the highest simulation accuracy, with the highest correlation coefficient (0.50 at Dye-2, and 0.62 at KAN_U), the highest NSE (0.18 at Dye-2, and 0.35 at KAN_U), and the smallest RMSE (107.01 kg m⁻³ at Dye-2, and 112.12 kg m⁻³ at KAN_U). At the Dye-2-17-2 core, each flow scheme exhibits density variability in the first 10 m and simulates an ice layer at around 3 m depth. In contrast, the schemes using Darcy's law and bucket percolation slightly underestimate the thickness of the ice layer (Fig. 9). At the KAN_U-13-1 core, none of the schemes reproduces the density

565   variability within the 7-11 m depth range. The scheme used in this study might compensate for high and low densities within this range, resulting in the model's overall performance closest to observations (-0.03% for mean density and 0.14% for

FAC). Both the Darcy-flow and bucket schemes exhibit density overestimation within this range, particularly the bucket

scheme, leading to the highest mean density (2.38%) and lowest FAC (-12.09%) among the three models.
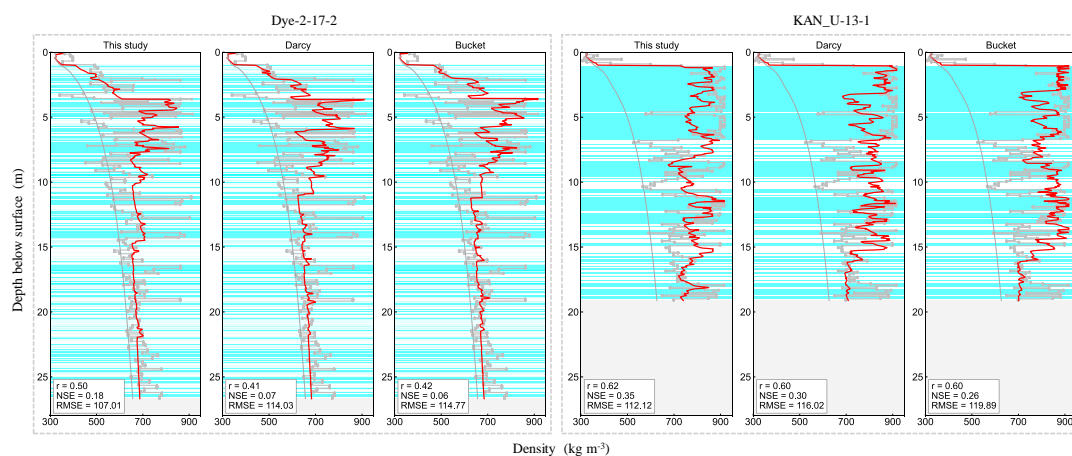
Figure 9. Observed (gray dotted line) and modelled (red solid line) firn depth-density profiles at the Dye-2-17-2 and KAN_U-13-1 cores. The modelled density profiles are driven by different percolation schemes. Ice layer stratigraphy is shown as cyan horizontal lines. The gray-shaded regions indicate no data. The thin inclined line denotes dry firn density simulated using the CROCUS model. The correlation coefficient (r), Nash-Sutcliffe efficiency coefficient (NSE), and root mean square error (RMSE) are displayed in the bottom left of each panel.

Table 9. Statistics and model outputs of firn density profiles at the Dye-2-17-2 and KAN_U-13-1 cores, including the mean firn density and FAC for the entire core depth range, relative bias in density and FAC. A slash indicates no data.

Core name	Model	Mean density (kg m⁻³)	Relative bias in density (%)	FAC (m)	Relative bias in FAC (%)
Dye-2-17-2	Observation	646.11	/	7.88	/
	This study	656.76	1.65	7.57	-3.93
	Darcy's law	655.17	1.40	7.62	-3.35
	Bucket acheme	663.13	2.64	7.39	-6.29
KAN_U-13-1	Observation	766.33	/	3.14	/
	This study	766.11	-0.03	3.15	0.14
	Darcy's law	767.00	0.09	3.13	-0.45
	Bucket acheme	784.55	2.38	2.76	-12.09

5.4 Comparison of time step sizes

The time step is an essential factor in firn densification models, representing the progression of time and the advection of firn

layers. At each time step, new snow accumulation is added as a new firn layer at the top of the firn column and firn density is

calculated based on the refreshed firn parameters such as layer mass, temperature, and liquid water content. In many

585   previous studies, the time step is set to a constant value, leading to a varied snow accumulation within each time step with different climatic conditions. For example, Verjans et al. (2019) and Vandecrux et al. (2020c) ran models with three-hourly time steps; Stevens et al. (2020) ran the CFM model with monthly time steps. We refer to this time-fixed model driving method as time-driven, which has a limitation that it may overlook the impact of short-term weather fluctuations on densification. A smaller amount of snowfall within a time step is more susceptible to being influenced by wind and is blown from the surface of the firn column. As a result, negative snowfall amounts occur within certain time steps in the

590   RACMO2.3p2 model, which are ignored in the time-driven method. Moreover, running the model with fewer snowfall amounts within a time step also increases the computational burden. Here, we run the model driven by accumulation, defining the time step sizes as the time required for the snow accumulation to reach a certain value, referred to as accumulation-driven. By waiting for the snow accumulation to reach a certain threshold before computation, it is possible to simulate the effects of accumulation on firn more accurately and reduce making biased predictions when snowfall amounts

595   are minimal or negative. Due to the significant computational resources required by Darcy's law and the extensive data needed to run daily time steps from 1958 to 2020, we compare results simulated using the bucket percolation scheme under both accumulation-driven and time-driven conditions.
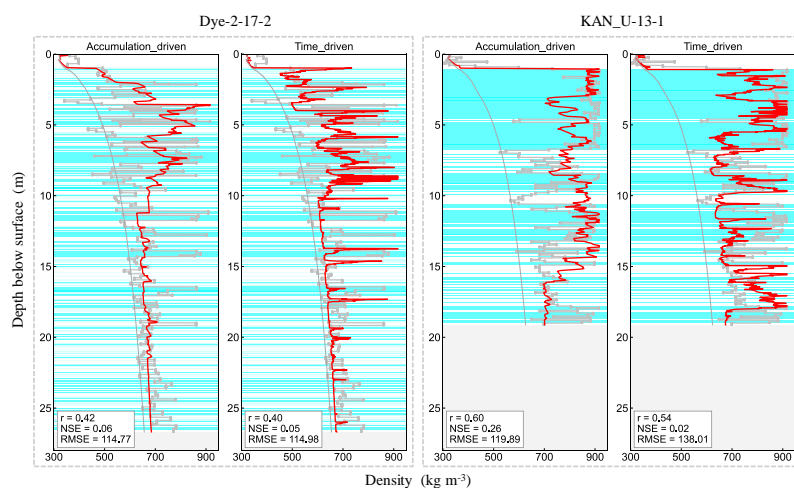
600   **Figure 10. Observed (gray dotted line) and modelled (red solid line) firn depth-density profiles at the Dye-2-17-2 and KAN_U-13-1 cores. The modelled density profiles are driven by accumulation and time, respectively. The gray-shaded regions indicate no data. The thin inclined line denotes dry firn density simulated using the CROCUS model. The correlation coefficient (r), Nash-Sutcliffe efficiency coefficient (NSE), and root mean square error (RMSE) are displayed in the bottom left of each panel.**

605   The accumulation-driven method successfully captures the high-density layers at KAN_U (Fig. 10), resulting in a smaller relative bias in density (2.38%) compared to that of the time-driven method (-6.77%) (Table 10). Moreover, this method also

simulates firn density relatively close to observations at Dye-2, with a relative density bias of 2.64%. At both sites, the time-driven method underestimates firn density, resulting in the modelled firn density being closer to the low-density peaks observed and the dry-firn density profiles, with a relative density bias of -1.79% at Dye-2 and -6.77% at KAN_U. This

610   underestimation is likely related to the lower amount of snowmelt during most time steps in the time-driven method and the limitations of matrix flow schemes. Specially, compared to schemes that account for preferential flow, a percolation scheme that only considers matrix flow is challenging to penetrate liquid water to greater depths (Vandecrux et al., 2020c; Verjans et al., 2019), inherently underestimating the liquid water refreezing. As a result, this scheme tends to perform better at sites with minimal snowmelt production, such as Dye-2. However, it encounters challenges in accurately capturing ice slab

615   formation at KAN_U, where liquid water is more abundant, leading to an underestimation of firn density at this site. Additionally, the scheme incorporating preferential flow produces overall results closer to observations at KAN_U, but it significantly overestimates firn density at Dye-2 (Sect. 5.1). In this study, the accumulation-driven method accumulated a certain amount of snowfall and snowmelt at each time step, potentially compensating for the inability of matrix flow to penetrate liquid water to deeper depths.

620

Table 10. Statistics and model outputs of firn density profiles at the Dye-2-17-2 and KAN_U-13-1 cores, including the mean firn density and FAC for the entire core depth range, relative bias in density and FAC. A slash indicates no data.

Core name	Model	Mean density (kg m^{-3})	Relative bias in density (%)	FAC (m)	Relative bias in FAC (%)
	Observation	646.11	/	7.88	/
Dye-2-17-2	Accumulation-driven	663.13	2.64	7.39	-6.29
	Time-driven	634.56	-1.79	8.22	4.26
	Observation	766.33	/	3.14	/
KAN_U-13-1	Accumulation-driven	784.55	2.38	2.76	-12.09
	Time-driven	714.43	-6.77	4.22	34.45

6 Conclusion

625   This study uses the CFM model as the foundational framework to simulate firn density at Dye-2 and KAN_U, two sites in the percolation zone of the southwest GrIS, with the model's upper boundary forced by the daily output of the region climate model RACMO2.3p2. The CROCUS compaction scheme and the Darcy-flow scheme are coupled to simulate firn properties. Various processes are considered in the firn densification model, including fresh-snow density variability, initial grain size variability, grain size growth, density-dependent and temperature-dependent thermal conductivity, dry-firn compaction, state-

630   dependent hydraulic conductivity, retention, refreezing, and runoff. The expression of the irreducible water in the Darcy-flow

scheme is modified by the parameterization of Coléou and Lesaffre (1998). Moreover, the time step is set to the time required for the accumulation to reach a specific value in this study rather than being set to a fixed interval (such as hours, days, weeks, months, or years).

635 Comparison with the in situ measurements obtained from 16 firn cores shows that the model in this study performs well at both Dye-2 and KAN_U, two climatologically distinct sites in the southwest percolation zone of the GrIS. At the minimal snowmelt production site of Dye-2, the model reproduces thin ice lenses or ice layers in the top 10 m of the firn column, which are caused by the increased snowmelt in recent years. The modelled firn density aligns with the average level of observations, with the relative bias in density ranging from 0.36% (Dye-2-13-2) to 6% (Dye-2-17-1). At the ice slab site of

640 KAN_U, the model captures the high-density firn layers and partly reproduces the observed ice slabs. For all 8 cores, the modelled density profiles compare well within uncertainties to observations, with a relative density bias being within ±5%. As indicated by comparisons of dry-firn densification schemes, water flow schemes, and time step sizes, the model used in this study exhibits good agreement within uncertainties with observations at both Dye-2 and KAN_U, possibly associated with the choice of time step. This study relates the time step with snow accumulation, which potentially compensates for the

645 limitation of the matrix flow scheme, enabling the model to capture the formation of high-density firn layers at KAN_U. Meanwhile, the nature of matrix flow enables the model in this study to exhibit good performance at Dye-2 as well.

Our study indicates that the high-density firn layers and overall characteristics of the upper firn density in the percolation zone could be captured by the choice of appropriate model configurations and climatic forcing data. However, the variability

650 in firn density has yet to be fully reproduced due to the limited understanding and knowledge gaps of densification processes in the presence of liquid water. For example, the overestimation of low-density peaks may be caused by the limited knowledge of how the ice lenses and/or ice layers persist in the deep firn layers after formation. The power-law creep mechanisms or shear forces may induce the newly formed thin ice lenses and/or ice layers to break, potentially leading to a lower firn density compared to the direct downward shift of ice lenses and/or ice layers. In future firn densification

655 modelling, machine learning methods should be considered to integrate data-driven and physical mechanisms, reducing uncertainties arising from poorly understood firn densification processes.

Code and Data availability. The RACMO2.3p2 data is available from Brice Noël without conditions (Noël et al., 2019). The Community Firn Model code is publicly available under the MIT license at https://doi.org/10.5281/zenodo.8083362 (Stevens

660 et al., 2023). The depth-density profiles and ice layer stratigraphy of 16 cores used in this study can be found at

https://doi.org/10.18739/A2NP1WK6M (Thompson et al., 2022) and http://doi.org/10.18739/A2CZ3263B (Xiao et al., 2022), respectively. The model outputs of Vandecrux et al. (2020c) are available online at https://doi.org/10.22008/FK2/CVPUJL (Vandecrux et al., 2020b). The codes and outputs of this study are available from the authors.

665 *Author contribution*. Xueyu Zhang completed the modelling work and wrote the original manuscript. Lin Liu designed the research together with Zhicai Luo and supervised the work. Brice Noël processed and provided the RACMO2.3p2 forcing data. All the authors contributed to the analysis, interpretation of the results and provided feedback on the final manuscript.

Competing interests. The authors declare that they have no conflict of interest.

670

Acknowledgements. This research was financially supported by the National Natural Science Foundation of China (grant nos. 42274028 and 41704023). Brice Noël was funded by the Fonds de la Recherche Scientifique de Belgique (F.R.S.-FNRS). We acknowledge Christopher Max Stevens for the open-source CFM model and his assistance in modelling the firn densification model. We would also like to thank Megan Thompson-Munson and Jing Xiao for compiling the available core data.

675

Refrences

Arthern, R. J., Vaughan, D. G., Rankin, A. M., Mulvaney, R., and Thomas, E. R.: In situ measurements of Antarctic snow compaction compared with predictions of models, J. Geophys. Res.-Earth, 115, F03011, https://doi.org/10.1029/2009JF001306, 2010.

680 Brils, M., Kuipers Munneke, P., van de Berg, W. J., and van den Broeke, M.: Improved representation of the contemporary Greenland ice sheet firn layer by IMAU-FDM v1.2G, Geosci. Model Dev., 15, 7121-7138, https://doi.org/10.5194/gmd-15-7121-2022, 2022.

Brun, E., David, P., Sudul, M., and Brunot, G.: A numerical model to simulate snow-cover stratigraphy for operational avalanche forecasting, J. Glaciol., 38, 13-22, https://doi.org/10.3189/S0022143000009552, 1992.

685 Calonne, N., Flin, F., Morin, S., Lesaffre, B., du Roscoat, S. R., and Geindreau, C.: Numerical and experimental investigations of the effective thermal conductivity of snow, Geophys. Res. Lett., 38, L23501, https://doi.org/10.1029/2011GL049234, 2011.

Calonne, N., Geindreau, C., Flin, F., Morin, S., Lesaffre, B., Rolland du Roscoat, S., and Charrier, P.: 3-D image-based numerical computations of snow permeability: links to specific surface area, density, and microstructural anisotropy, The

690   Cryosphere, 6, 939-951, https://doi.org/10.5194/tc-6-939-2012, 2012.

Calonne, N., Milliancourt, L., Burr, A., Philip, A., Martin, C. L., Flin, F., and Geindreau, C.: Thermal conductivity of snow, firn, and porous ice from 3-D image-based computations, Geophys. Res. Lett., 46, 13079-13089, https://doi.org/10.1029/2019GL085228, 2019.

Colbeck, S. C.: The capillary effects on water percolation in homogeneous snow, J. Glaciol., 13, 85-97,

695   https://doi.org/10.3189/S002214300002339X, 1974.

Colbeck, S. C.: A theory for water flow through a layered snowpack, Water Resour. Res., 11, 261-266, https://doi.org/10.1029/WR011i002p00261, 1975.

Coléou, C. and Lesaffre, B.: Irreducible water saturation in snow: experimental results in a cold laboratory, Ann. Glaciol., 26, 64-68, https://doi.org/10.3189/1998AoG26-1-64-68, 1998.

700   Cuffey, K. M. and Paterson, W. S. B.: The Physics of Glaciers, 4th ed., Pergamon, Oxford, U. K, 693 pp., ISBN 978-0-12-369461-4, 2010.

Enderlin, E. M., Howat, I. M., Jeong, S., Noh, M.-J., Angelen, J. H., and Broeke, M. R.: An improved mass budget for the Greenland ice sheet, Geophys. Res. Lett., 41, 866-872, https://doi.org/10.1002/2013GL059010, 2014.

Fausto, R. S., Box, J. E., Vandecrux, B., van As, D., Steffen, K., MacFerrin, M. J., Machguth, H., Colgan, W., Koenig, L. S.,

705   McGrath, D., Charalampidis, C., and Braithwaite, R. J.: A Snow Density Dataset for Improving Surface Boundary Conditions in Greenland Ice Sheet Firn Modeling, Front. Earth Sci., 6, 40-49, https://doi.org/10.3389/feart.2018.00051, 2018.

Fettweis, X., Hofer, S., Krebs-Kanzow, U., Amory, C., Aoki, T., Berends, C. J., Born, A., Box, J. E., Delhasse, A., Fujita, K., Gierz, P., Goelzer, H., Hanna, E., Hashimoto, A., Huybrechts, P., Kapsch, M.-L., King, M. D., Kittel, C., Lang, C.,

710   Langen, P. L., Lenaerts, J. T. M., Liston, G. E., Lohmann, G., Mernild, S. H., Mikolajewicz, U., Modali, K., Mottram, R. H., Niwano, M., Noël, B., Ryan, J. C., Smith, A., Streffing, J., Tedesco, M., van de Berg, W. J., van den Broeke, M., van de Wal, R. S. W., van Kampenhout, L., Wilton, D., Wouters, B., Ziemen, F., and Zolles, T.: GrSMBMIP: intercomparison of the modelled 1980-2012 surface mass balance over the Greenland Ice Sheet, The Cryosphere, 14, 3935-3958, https://doi.org/10.5194/tc-14-3935-2020, 2020.

715   Forster, R. R., Box, J. E., van den Broeke, M. R., Miège, C., Burgess, E. W., van Angelen, J. H., Lenaerts, J. T. M., Koenig, L. S., Paden, J., Lewis, C., Gogineni, S. P., Leuschen, C., and McConnell, J. R.: Extensive liquid meltwater storage in firn within the Greenland ice sheet, Nat. Geosci., 7, 95-98, https://doi.org/10.1038/ngeo2043, 2014.

Gow, A. J.: On the Rates of Growth of Grains and Crystals in South Polar Firn, J. Glaciol., 8, 241-252, https://doi.org/10.3189/S0022143000031233, 1969.

720 Harper, J., Humphrey, N., Pfeffer, W. T., Brown, J., and Fettweis, X.: Greenland ice-sheet contribution to sea-level rise buffered by meltwater storage in firn, Nature, 491, 240-243, https://doi.org/10.1038/nature11566, 2012.

Herron, M. M. and Langway, C. C.: Firn densification: an empirical model., J. Glaciol., 25, 373-385, https://doi.org/10.1017/S0022143000015239, 1980.

Hirashima, H., Yamaguchi, S., Sato, A., and Lehning, M.: Numerical modeling of liquid water movement through layered

725 snow based on new measurements of the water retention curve, Cold Reg. Sci. Technol., 64, 94-103, https://doi.org/10.1016/j.coldregions.2010.09.003, 2010.

Humphrey, N. F., Harper, J. T., and Pfeffer, W. T.: Thermal tracking of meltwater retention in Greenland's accumulation area, J. Geophys. Res.-Earth Surf., 117, 1-11, https://doi.org/10.1029/2011JF002083, 2012.

Huss, M.: Density assumptions for converting geodetic glacier volume change to mass change, The Cryosphere, 7, 877-887,

730 https://doi.org/10.5194/tc-7-877-2013, 2013.

Katsushima, T., Kumakura, T., and Takeuchi, Y.: A multiple snow layer model including a parameterization of vertical water channel process in snowpack, Cold Reg. Sci. Technol., 59, 143-151, https://doi.org/10.1016/j.coldregions.2009.09.002, 2009.

Keenan, E., Wever, N., Dattler, M., Lenaerts, J. T. M., Medley, B., Kuipers Munneke, P., and Reijmer, C.: Physics-based

735 SNOWPACK model improves representation of near-surface Antarctic snow and firn density, The Cryosphere, 15, 1065-1085, https://doi.org/10.5194/tc-15-1065-2021, 2021.

Kuipers Munneke, P., Ligtenberg, S. R. M., Noël, B. P. Y., Howat, I. M., Box, J. E., Mosley-Thompson, E., McConnell, J. R., Steffen, K., Harper, J. T., Das, S. B., and van den Broeke, M. R.: Elevation change of the Greenland Ice Sheet due to surface mass balance and firn processes, 1960-2014, The Cryosphere, 9, 2009-2025, https://doi.org/10.5194/tc-9-2009-

740 2015, 2015.

Langen, P. L., Fausto, R. S., Vandecrux, B., Mottram, R. H., and Box, J. E.: Liquid Water Flow and Retention on the Greenland Ice Sheet in the Regional Climate Model HIRHAM5: Local and Large-Scale Impacts, Front. Earth Sci., 4, 110, https://doi.org/10.3389/feart.2016.00110, 2017.

Ligtenberg, S. R. M., Helsen, M. M., and van den Broeke, M. R.: An improved semi-empirical model for the densification of

745 Antarctic firn, The Cryosphere, 5, 809-819, https://doi.org/10.5194/tc-5809-2011, 2011.

Ligtenberg, S. R. M., Kuipers Munneke, P., Noël, B. P. Y., and van den Broeke, M. R.: Brief communication: Improved simulation of the present-day Greenland firn layer (1960-2016), The Cryosphere, 12, 1643-1649, https://doi.org/10.5194/tc-12-1643-2018, 2018.

Linow, S., Hörhold, M., and Freitag, J.: Grain-size evolution of polar firn: A new empirical grain growth parameterization
750   based on X-ray microcomputer tomography measurements, J. Glaciol., 58, 1245-1252, https://doi.org/10.3189/2012JoG11J256, 2012.

MacFerrin, M. J., Stevens, C. M., Vandecrux, B., Waddington, E. D., and Abdalati, W.: The Greenland Firn Compaction Verification and Reconnaissance (FirnCover) dataset, 2013-2019, Earth Syst. Sci. Data, 14, 955-971, https://doi.org/10.5194/essd-14955-2022, 2022.

755   MacFerrin, M., Machguth, H., van As, D., Charalampidis, C., Stevens, C. M., Heilig, A., Vandecrux, B., Langen, P. L., Mottram, R., Fettweis, X., Van den Broeke, M. R., Pfeffer, W. T., Moussavi, M., and Abdalati, W.: Rapid expansion of Greenland's low-permeability ice slabs, Nature, 573, 403-407, https://doi.org/10.1038/s41586-019-1550-3, 2019.

Machguth, H., MacFerrin, M., van As, D., Box, J. E., Charalampidis, C., Colgan, W., Fausto, R. S., Meijer, H. A. J., Mosley-Thompson, E., and van de Wal, R. S. W.: Greenland meltwater storage in firn limited by near-surface ice formation, Nat.
760   Clim. Change, 6, 390-393, https://doi.org/10.1038/nclimate2899, 2016.

Marchenko, S., Van Pelt, W. J. J., Claremar, B., Pohjola, V., Pettersson, R., Machguth, H., and Reijmer, C.: Parameterizing deep water percolation improves subsurface temperature simulations by a multilayer firn model, Front. Earth Sci., 5, 16, https://doi.org/10.3389/feart.2017.00016, 2017.

McMillan, M., Leeson, A., Shepherd, A., Briggs, K., Armitage, T. W., Hogg, A., Kuipers Munneke, P., van den Broeke, M.,
765   Noël, B., van de Berg, W. J., Ligtenberg, S., Horwath, M., Groh, A., Muir, A., and Gilbert, L.: A high-resolution record of Greenland mass balance, Geophys. Res. Lett., 43, 7002-7010, https://doi.org/10.1002/2016GL069666, 2016.

Meyer, C. R. and Hewitt, I. J.: A continuum model for meltwater flow through compacting snow, The Cryosphere, 11, 2799-2813, https://doi.org/10.5194/tc-11-2799-2017, 2017.

Morris, E. M. and Wingham, D. J.: Uncertainty in massbalance trends derived from altimetry: a case study along the EGIG
770   line, central Greenland, J. Glaciol., 61, 345-356, https://doi.org/10.3189/2015JoG14J123, 2015.

Mottram, R., Simonsen, S. B., Svendsen, S. H., Barletta, V. R., Sørensen, L. S., Nagler, T., Wuite, J., Groh, A., Horwath, M., Rosier, J., Solgaard, A., Hvidberg, C. S., and Forsberg, R.: An Integrated View of Greenland Ice Sheet Mass Changes Based on Models and Satellite Observations, Remote Sens., 11, 1-26, https://doi.org/10.3390/rs11121407, 2019.

Mualem, Y.: A new model for predicting the hydraulic conductivity of unsaturated porous media, Water Resour. Res., 12,
775   513-522, https://doi.org/10.1029/WR012i003p00513, 1976.

Nash, J. E. and Sutcliffe, J. V.: River flow forecasting through conceptual models part I - A discussion of principles, J. Hydrol., 10, 282-290, https://doi.org/10.1016/0022-1694(70)90255-6, 1970.

Nghiem, S. V., Hall, D. K., Mote, T. L., Tedesco, M., Albert, M. R., Keegan, K., Shuman, C. A., DiGirolamo, N. E., and Neumann, G.: The extreme melt across the Greenland ice sheet in 2012, Geophys. Res. Lett., 39, 6-11, https://doi.org/10.1029/2012GL053611, 2012.

Noël, B., van de Berg, W. J., van Wessem, J. M., van Meijgaard, E., van As, D., Lenaerts, J. T. M., Lhermitte, S., Kuipers Munneke, P., Smeets, C. J. P. P., van Ulft, L. H., van de Wal, R. S. W., and van den Broeke, M. R.: Modelling the climate and surface mass balance of polar ice sheets using RACMO2 - Part 1: Greenland (1958-2016), The Cryosphere, 12, 811-831, https://doi.org/10.5194/tc-12-811-2018, 2018.

Noël, B., van de Berg, W. J., Lhermitte, S., and van den Broeke, M. R.: Rapid ablation zone expansion amplifies north Greenland mass loss, Sci. Adv., 5, 2-11, https://doi.org/10.1126/sciadv.aaw0123, 2019.

Patankar, S. V.: Numerical heat transfer and fluid flow, CRC Press, Boca Raton, https://doi.org/10.1201/9781482234213, 1980.

Pfeffer, W. T. and Humphrey, N. F.: Determination of timing and location of water movement and ice-layer formation by temperature measurements in sub-freezing snow, J. Glaciol., 42, 292-304, https://doi.org/10.3189/S0022143000004159, 1996.

Pfeffer, W. T., Meier, M. F., and Illangasekare, T. H.: Retention of Greenland runoff by refreezing: Implications for projected future sea level change, J. Geophys. Res.-Oceans, 96, 22117-22124, https://doi.org/10.1029/91JC02502, 1991.

Reijmer, C. H., van den Broeke, M. R., Fettweis, X., Ettema, J., and Stap, L. B.: Refreezing on the Greenland ice sheet: a comparison of parameterizations, The Cryosphere, 6, 743-62, https://doi.org/10.5194/tc-6-743-2012, 2012.

Ren, J.-W., Sheng, Y., et al.: The physics of cryosphere, 1st ed., Science press, Beijing, 150 pp., ISBN 978-7-03-066724-3, 2020.

Rennermalm, Å. K., Hock, R., Covi, F., Xiao, J., Corti, G., Kingslake, J., Leidman, S. Z., Miège, C., Macferrin, M., Machguth, H., Osterberg, E., Kameda, T., McConnell, J. R.: Shallow firn cores 1989-2019 in southwest Greenland's percolation zone reveal decreasing density and ice layer thickness after 2012. J. Glaciol. 68, 431-442. https://doi.org/10.1017/jog.2021.102, 2021.

Richards, L.: Capillary conduction of liquids through porous mediums, J. Appl. Phys., 1, 318-333, https://doi.org/10.1063/1.1745010, 1931.

Rignot, E., Mouginot, J., Scheuchl, B., Van Den Broeke, M., Van Wessem, M. J., and Morlighem, M.: Four decades of

805   Antarctic Ice Sheet mass balance from 1979-017, P. Natl. Acad. Sci. USA, 116, 1095-1103,

https://doi.org/10.1073/pnas.1812883116, 2019.

Schwerdtfeger, P.: Theoretical derivation of the thermal conductivity and diffusivity of snow, International Association of

Hydrological Sciences Publication, 61, 75-81, 1963.

Shepherd, A., Ivins, E. R., Geruo, A., Barletta, V. R., Bentley, M. J., Bettadpur, S., Briggs, K. H., Bromwich, D. H.,

810   Forsberg, R., and Galin, N.: A reconciled estimate of ice-sheet mass balance, Science, 338, 1183-1189,

https://doi.org/10.1126/science.1228102, 2012.

Shepherd, A., Ivins, E., Rignot, E., Smith, B., van den Broeke, M., Velicogna, I., Whitehouse, P., Briggs, K., Joughin, I.,

Krinner, G., Nowicki, S., Payne, T., Scambos, T., Schlegel, N., A, G., Agosta, C., Ahlstrøm, A., Babonis, G., Barletta, V.

R., Bjørk, A. A., Blazquez, A., Bonin, J., Colgan, W., Csatho, B., Cullather, R., Engdahl, M. E., Felikson, D., Fettweis, X.,

815   Forsberg, R., Hogg, A. E., Gallee, H., Gardner, A., Gilbert, L., Gourmelen, N., Groh, A., Gunter, B., Hanna, E., Harig, C.,

Helm, V., Horvath, A., Horwath, M., Khan, S., Kjeldsen, K. K., Konrad, H., Langen, P. L., Lecavalier, B., Loomis, B.,

Luthcke, S., McMillan, M., Melini, D., Mernild, S., Mohajerani, Y., Moore, P., Mottram, R., Mouginot, J., Moyano, G.,

Muir, A., Nagler, T., Nield, G., Nilsson, J., Noël, B., Otosaka, I., Pattle, M. E., Peltier, W. R., Pie, N., Rietbroek, R., Rott,

H., Sandberg Sørensen, L., Sasgen, I., Save, H., Scheuchl, B., Schrama, E., Schröder, L., Seo, K. W., Simonsen, S. B.,

820   Slater, T., Spada, G., Sutterley, T., Talpe, M., Tarasov, L., van de Berg, W. J., van der Wal, W., van Wessem, M.,

Vishwakarma, B. D., Wiese, D., Wilton, D., Wagner, T., Wouters, B., and Wuite, J.: Mass balance of the Greenland Ice

Sheet from 1992 to 2018, Nature, 579, 233-239, https://doi.org/10.1038/s41586-019-1855-2, 2020.

Shimizu, H.: Air permeability of deposited snow, Contribut. Instit. Low Temp. Sci., A22, 1-32,

http://hdl.handle.net/2115/20234, 1970.

825   Simonsen, S. B., Stenseng, L., Adalgeirsdottir, G., Fausto, R. S., Hvidberg, C. S., and Lucas-Picher, P.: Assessing a

multilayered dynamic firn-compaction model for Greenland with ASIRAS radar measurements, J. Glaciol., 59, 545-558,

https://doi.org/10.3189/2013JoG12J158, 2013.

Smith, B., Fricker, H. A., Gardner, A. S., Medley, B., Nilsson, J., Paolo, F. S., Holschuh, N., Adusumilli, S., Brunt, K., and

Csatho, B.: Pervasive ice sheet mass loss reflects competing ocean and atmosphere processes, Science, 368, 1239-1242,

830   https://doi.org/10.1126/science.aaz5845, 2020.

Sørensen, L. S., Simonsen, S. B., Nielsen, K., Lucas-Picher, P., Spada, G., Adalgeirsdottir, G., Forsberg, R., and Hvidberg, C.

S.: Mass balance of the Greenland ice sheet (2003-2008) from ICESat data - the impact of interpolation, sampling and firn

density, The Cryosphere, 5, 173-186, https://doi.org/10.5194/tc-5173-2011, 2011.

Steger, C. R., Reijmer, C. H., and van den Broeke, M. R.: The modelled liquid water balance of the Greenland Ice Sheet, The

835 Cryosphere, 11, 2507-2526, https://doi.org/10.5194/tc-11-25072017, 2017.

Stevens, C. M., Verjans, V., Lundin, J. M. D., Kahle, E. C., Horlings, A. N., Horlings, B. I., and Waddington, E. D.: The

Community Firn Model (CFM) v1.0, Geosci. Model Dev., 13, 4355-4377, https://doi.org/10.5194/gmd-13-4355-2020,

2020.

Stevens, C. M., Vo, H., emmakahle, Jboat, and oraschewski: UWGlaciology/CommunityFirnModel: Version 2.2.0, Zenodo

840 [code], https://doi.org/10.5281/zenodo.8083362, 2023.

Sturm, M., Holmgren, J., König, M., and Morris, K.: The thermal conductivity of seasonal snow, J. Glaciol., 43, 26-41,

https://doi.org/10.3189/S0022143000002781, 1997.

Thompson-Munson, M., Montgomery, L., Lenaerts, J., and Koenig, L.: Surface Mass Balance and Snow Depth on Sea Ice

Working Group (SUMup) snow density subdataset, Greenland and Antartica, 1952-2019, Arctic Data Center [data set],

845 https://doi.org/10.18739/A2NP1WK6M, 2022.

Thompson-Munson, M., Wever, N., Stevens, C. M., Lenaerts, J. T. M., and Medley, B.: An evaluation of a physics-based

firn model and a semi-empirical firn model across the Greenland Ice Sheet (1980-2020), The Cryosphere, 17, 2185-2209,

https://doi.org/10.5194/tc-17-2185-2023, 2023.

van Angelen, J. H., M. Lenaerts, J. T., van den Broeke, M. R., Fettweis, X., and van Meijgaard, E.: Rapid loss of firn pore

850 space accelerates 21st century Greenland mass loss, Geophys. Res. Lett., 40, 2109-2113,

https://doi.org/10.1002/grl.50490, 2013.

van Dalum, C. T., van de Berg, W. J., and van den Broeke, M. R.: Impact of updated radiative transfer scheme in snow and

ice in RACMO2.3p3 on the surface mass and energy budget of the Greenland ice sheet, The Cryosphere, 15, 1823-1844,

https://doi.org/10.5194/tc-15-1823-2021, 2021.

855 van den Broeke, M. R., Enderlin, E. M., Howat, I. M., Kuipers Munneke, P., Noël, B. P. Y., van de Berg, W. J., van

Meijgaard, E., and Wouters, B.: On the recent contribution of the Greenland ice sheet to sea level change, The

Cryosphere, 10, 1933-1946, https://doi.org/10.5194/tc-10-1933-2016, 2016.

van den Broeke, M., Bamber, J., Ettema, J., Rignot, E., Schrama, E., Van Berg, W. J. D., Van Meijgaard, E., Velicogna, I.,

and Wouters, B.: Partitioning recent Greenland mass loss, Science, 326, 984-986,

860 https://doi.org/10.1126/science.1178176, 2009.

van Dusen, M. S., and Washburn, E. W.: Thermal conductivity of non-metallic solids, International critical tables of

numerical data, physics, chemistry and technology, New York: McGraw-Hill, 216-217, 1929.

van Genuchten, M.: A closed form equation for predicting the hydraulic conductivity of unsaturated soils., Soil Sci. Soc. Am. J., 44, 892-898, https://doi.org/10.2136/sssaj1980.03615995004400050002x, 1980.

865   van Kampenhout, L., Lenaerts, J. T. M., Lipscomb, W. H., Sacks, W. J., Lawrence, D. M., Slater, A. G., and van den Broeke, M. R.: Improving the representation of polar snow and firn in the Community Earth System Model. J. Adv. Model. Earth Sy., 9, 2583-2600, https://doi.org/10.1002/2017MS000988, 2017.

van Pelt, W. J. J., Oerlemans, J., Reijmer, C. H., Pohjola, V. A., Pettersson, R., and van Angelen, J. H.: Simulating melt, runoff and refreezing on Nordenskiöldbreen, Svalbard, using a coupled snow and energy balance model, The

870   Cryosphere, 6, 641-659, https://doi.org/10.5194/tc-6-641-2012, 2012.

van Pelt, W., Pohjola, V., Pettersson, R., Marchenko, S., Kohler, J., Luks, B., Hagen, J. O., Schuler, T. V., Dunse, T., Noël, B., and Reijmer, C.: A long-term dataset of climatic mass balance, snow conditions, and runoff in Svalbard (1957-2018), The Cryosphere, 13, 2259-2280, https://doi.org/10.5194/tc-13-22592019, 2019.

Vandecrux, B., Fausto, R. S., Langen, P. L., van As, D., MacFerrin, M., Colgan, W. T., Ingeman-Nielsen, T., Steffen, K.,

875   Jensen, N. S., Møller, M. T., and Box, J. E.: Drivers of Firn Density on the Greenland Ice Sheet Revealed by Weather Station Observations and Modeling, J. Geophys. Res.-Earth Surf., 123, 2563-2576, https://doi.org/10.1029/2017JF004597, 2018.

Vandecrux, B., MacFerrin, M., Machguth, H., Colgan, W. T., van As, D., Heilig, A., Stevens, C. M., Charalampidis, C., Fausto, R. S., Morris, E. M., Mosley-Thompson, E., Koenig, L., Montgomery, L. N., Miège, C., Simonsen, S. B.,

880   Ingeman-Nielsen, T., and Box, J. E.: Firn data compilation reveals widespread decrease of firn air content in western Greenland, The Cryosphere, 13, 845-859, https://doi.org/10.5194/tc-13-845-2019, 2019.

Vandecrux, B., Fausto, R. S., van As, D., Colgan, W., Langen, P. L., Haubner, K., Ingeman-Nielsen, T., Heilig, A., Stevens, C. M., MacFerrin, M., Niwano, M., Steffen, K., and Box, J.: Firn cold content evolution at nine sites on the Greenland ice sheet between 1998 and 2017, J. Glaciol., 66, 1-12, https://doi.org/10.1017/jog.2020.30, 2020a.

885   Vandecrux, B., Langen, P.L., Kuipers Munneke, P. Simonsen, S., Verjans, Stevens, C. M. V., Marchenko, S., Van Pelt, W., and Meyer, C.: The firn meltwater retention model intercomparison project (RetMIP): model outputs, GEUS, https://doi.org/10.22008/FK2/CVPUJL, 2020b.

Vandecrux, B., Mottram, R., Langen, P. L., Fausto, R. S., Olesen, M., Stevens, C. M., Verjans, V., Leeson, A., Ligtenberg, S., Kuipers Munneke, P., Marchenko, S., van Pelt, W., Meyer, C. R., Simonsen, S. B., Heilig, A., Samimi, S., Marshall,

890   S., Machguth, H., MacFerrin, M., Niwano, M., Miller, O., Voss, C. I., and Box, J. E.: The firn meltwater Retention Model Intercomparison Project (RetMIP): evaluation of nine firn models at four weather station sites on the Greenland ice sheet, The Cryosphere, 14, 3785-3810, https://doi.org/10.5194/tc-14-3785-2020, 2020c.

Veldhuijsen, S. B. M., van de Berg, W. J., Brils, M., Kuipers Munneke, P., and van den Broeke, M. R.: Characteristics of the 1979-2020 Antarctic firn layer simulated with IMAU-FDM v1.2A, The Cryosphere, 17, 1675-1696, https://doi.org/10.5194/tc-17-1675-2023, 2023.

Verjans, V., Leeson, A. A., Stevens, C. M., MacFerrin, M., Noël, B., and van den Broeke, M. R.: Development of physically based liquid water schemes for Greenland firn-densification models, The Cryosphere, 13, 1819-1842, https://doi.org/10.5194/tc-13-1819-2019, 2019.

Vionnet, V., Brun, E., Morin, S., Boone, A., Faroux, S., Le Moigne, P., Martin, E., and Willemet, J. M.: The detailed snowpack scheme CROCUS and its implementation in SURFEX v7.2, Geosci. Model Dev., 5, 773-791, https://doi.org/10.5194/gmd-5773-2012, 2012.

Xiao, J., Covi, F., Rennermalm, Å. K., and Hock, R.: Data from: Resampled density in 48 shallow firn cores from Southwest Greenland, 2012-2019, Arctic Data Center, https://doi.org/10.18739/A2CZ3263B, 2022.

Yamaguchi, S., Katsushima, T., Sato, A., and Kumakura, T.: Water retention curve of snow with different grain sizes, Cold Reg. Sci. Technol., 64, 87-93. https://doi.org/10.1016/j.coldregions.2010.05.008, 2010.

Yen, Y.-C.: Review of the thermal properties of snow, ice and sea ice, Tech. Rep. 81-10, Cold Regions Research and Engineering Laboratory, Hanover, NH, USA, 27 pp. 1981.